8-2018

Experiments of Propeller-Induced Flow Effects on a Low-Reynolds-Number Wing

Gavin K. Ananda
University of Illinois

Robert Deters
Embry-Riddle Aeronautical University, DETERSR1@erau.edu

Michael S. Selig
University of Illinois, m-selig@illinois.edu

Experiments of Propeller-Induced Flow Effects on a Low-Reynolds-Number Wing

Gavin K. Ananda* and Michael S. Selig†
University of Illinois at Urbana–Champaign, Urbana, Illinois 61801
and
Robert W. Deters‡
Embry-Riddle Aeronautical University, Daytona Beach, Florida 32114

Novel findings are discussed in this paper that will be especially beneficial to designers and modelers of small-scale unmanned air vehicles and high-altitude long-endurance vehicles that both operate at low Reynolds numbers (Re = 50,000–300,000). Propeller-induced flow effects in both tractor and pusher configurations on a rectangular wing using the Wortmann FX 63-137 airfoil (a common low-Reynolds-number high-lift airfoil) are presented in this paper. Significant performance benefits can be found for a wing in the tractor configuration. Experiments, including trip tests and upper-surface oil flow visualization, show and verify that the propeller slipstream induces early transition to turbulent flow in the regions within the slipstream and the premature formation of a separation bubble in the regions outside the slipstream. The result is a reduction of pressure drag and an increase in lift of the wing where lift-to-drag ratios are as high as 10–12 (a maximum of 70% increase in lift-to-drag ratio from a clean wing configuration) and are measured at both low and high angles of attack up to stall (0–16 deg). Similar performance benefits are not observed in pusher configuration results where only increased local flow velocity and varying inflow angle effects are apparent. Thus, contrary to the design rules for optimal performance of wings at high Reynolds numbers, at low Reynolds numbers, a propeller in the tractor configuration exhibits significant performance improvements, especially in cruise configurations (low angles of attack), as compared with a propeller in the pusher configuration or even a clean wing.

Nomenclature

AR	=	aspect ratio
b	=	wingspan
C_D	=	wing drag coefficient; $D/(1/2)\rho V_\infty^2 S_{\text{ref}}$
C_L	=	wing lift coefficient; $L/(1/2)\rho V_\infty^2 S_{\text{ref}}$
$C_{M_{c/4}}$	=	wing pitching moment coefficient at quarter-chord; $M/(1/2)\rho V_\infty^2 S_{\text{ref}} c$
C_P	=	propeller power coefficient; $P/\rho n^3 D^5$
C_T	=	propeller thrust coefficient; $T/\rho n^2 D^4$
c	=	rectangular wing aerodynamic chord
D	=	propeller diameter, drag
J	=	propeller advance ratio; V_∞/nD
L	=	lift
M	=	pitching moment
n	=	propeller rotation rate in rotations per second
Q	=	propeller torque
R	=	propeller radius
Re	=	Reynolds number; $V_\infty c/\nu$ or $V_{75\%R} c_{75\%R}/\nu$
S_{ref}	=	wing reference area
T/A	=	propeller disk loading
V_∞	=	freestream velocity
w	=	propeller axial induced velocity
α	=	wing angle of attack
η	=	propeller efficiency; $C_T J/C_P$
λ	=	taper ratio
ν	=	kinematic viscosity
ρ	=	density of air
Ω	=	propeller rotation rate

*Ph.D. Candidate, Department of Aerospace Engineering; anandak1@illinois.edu. Student Member AIAA.

†Professor Emeritus, Department of Aerospace Engineering; m-selig@illinois.edu. Associate Fellow AIAA.

‡Assistant Professor, Department of Engineering and Technology; detersr1@erau.edu. Member AIAA.

I. Introduction

THE flow induced by a propeller refers to either the inflow or outflow (slipstream) of a propeller. With the current widespread use of small-scaled unmanned air vehicles (UAVs) and increased interest in distributed electric propulsion aircraft, much emphasis is being placed into properly understanding wing performance characteristics when subject to propeller-induced flow conditions. The main goal of this research area is to ensure that the benefits of proper propeller–wing integration are maximized when designing small-scale UAVs.

The effect of propeller-induced flow on the aerodynamic performance of a wing has been a subject of detailed research since the 1940s and 1950s [1–7]. More recently, research has been conducted into the proper integration of the propeller–wing combination. In 1984, Loth and Loth [8] proposed that wing-induced drag could be reduced through the use of wingtip mounted propellers. The induced drag-mitigating effects of wingtip-mounted propellers was confirmed experimentally and modeled numerically by Patterson and Bartlett [9] and Miranda and Brennan [10], respectively. Propeller–wing integration was taken a step further by Kroo [11], who proposed that the wings designed for tractor configuration aircraft should be optimized based on the power-on propeller setting and not a clean wing. From Munk's stagger theorem [12], Kroo [11] showed that, to minimize induced drag, the wing airfoil section geometry, chord, and twist distribution should be modified for optimal lift distribution in the propeller-on configurations. Veldhuis [13,14] advanced similar assertions to Kroo [11] when he performed detailed experimental and numerical investigations into tractor configuration propeller–wing tests at a Reynolds number of approximately 400,000. In addition, from propeller positioning parametric studies, Veldhuis [13,14] found that higher vertical positions and negative propeller inclination angles with respect to the wing provided beneficial results.

Important steady-state propeller–wing interaction studies were also performed by Witkowski et al. [15,16] and Catalano [17]. Witkowski et al. [15,16] showed aerodynamic performance improvements for wings under tractor configuration slipstream conditions. Tests performed on a semispan wing at a Reynolds number of 470,000 showed typical lift curve slope increases of approximately 5.6% and drag reductions of approximately 65% at maximum propeller power. In addition, the effect of the wing on the aerodynamic characteristics of the propeller was found to be minimal. Catalano [17] performed experiments on the effects of propeller-induced flow on the aerodynamics of a Wortmann FX 63-137 wing at Reynolds numbers of 350,000 and 450,000. Both pusher and tractor configurations were tested at varying positions and inclination angles. The results showed that, for tractor configuration cases within the region of the slipstream, transition occurred close to the leading edge of the wing, whereas for the pusher configuration, transition to turbulent flow was delayed.

The research discussed heretofore deals primarily with Reynolds numbers greater than 350,000. However, currently operational small-scaled UAVs and high-altitude long-endurance aircraft tend to operate in the flight regime ($Re = 30{,}000$–$300{,}000$) that is primarily hampered by the adverse low-Reynolds-number effects of the laminar separation bubble. Vehicles operating in this regime tend to be relatively inefficient (relatively low lift-to-drag ratios) and difficult to predict [18]. In addition, most operational small-scaled UAVs are of low-to-moderate aspect ratios ($2 \leq \mathcal{R} \leq 7$), and therefore tend to have a significant portion of their wing located in the propeller-induced flow region. The possible interactions between the three-dimensional wing effects, low-Reynolds-number effects, and the induced flow effects of the propeller in a small-scale UAV make it necessary to warrant further attention into the potential for performance improvements when performing propeller–wing integration.

At low Reynolds numbers, the effects of the induced flow of a propeller have been mainly researched experimentally on low-aspect-ratio ($\mathcal{R} \leq 2$) micro air vehicles. The Micro Air Vehicle group at the University of Arizona has performed experimental testing of single and contrarotating tractor-mounted propellers on low-aspect-ratio wings at Reynolds numbers between 50,000 to 100,000 [19–22]. The experimental results showed separation delay due to propeller slipstream flow and that, at higher angles of attack, higher lift-to-drag ratio values were observed in comparison with wing-only results. Flow visualization studies performed by Sudhakar et al. [23] also confirmed the separation delay effects discussed prior.

The limited amount of literature at low Reynolds numbers suggests that there is a need to expand the understanding of propeller-induced flow effects on wings at low Reynolds numbers given that laminar separation bubble effects are critical to wing performance. To accomplish this goal, experiments are conducted with a Wortmann FX 63-137 rectangular wing with an aspect ratio of four at Reynolds numbers from 60,000 to 90,000. Experiments are performed using multiple propellers in both tractor and pusher configurations at various advance ratios. The propellers used vary in diameter, blade planform, pitch, and number of blades to determine what effects the differences in propellers might have. The wind-tunnel results are also accompanied by trip tests and oil flow visualization results to help better understand the effects observed.

II. Experimental Methodology

A. Test Setup

Experiments were conducted at the low turbulence subsonic wind tunnel located at the Aerodynamic Research Laboratory at the University of Illinois at Urbana–Champaign, which has an open-return tunnel with a rectangular test section. The test section measures 2.8×4.0 ft (0.853×1.219 m) in cross section and 8 ft (2.438 m) in length, and it reaches speeds up to 160 mph (71.53 m/s). The turbulence intensity of the wind-tunnel test section is measured to be less than 0.1% [24].

The experimental setup consisted of two main independent components: a three-component platform force balance designated the low Reynolds number force balance (LRN-FB), and the propeller mounting structure as depicted in Fig. 1. The LRN-FB measured the aerodynamic loads of only the wing. The LRN-FB was a custom-designed and in-house-fabricated external three-component platform force balance. The design, assembly, and validation of the LRN-FB were described in detail in Refs. [25,26].

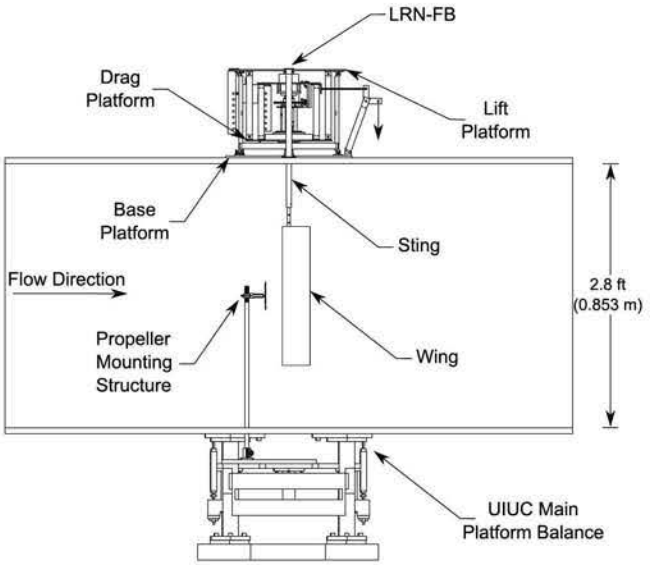

Fig. 1 UIUC LRN-FB and propeller mounting structure in the tractor configuration.

The propeller mounting structure provided the wing with the specific propeller-induced flow conditions. Shown in Fig. 2, the propeller mounting structure consists of five main components, namely, the mounting plates (component A), the square-flange mounts (component B), the vertically placed connecting rods (component C), the horizontally mounted nacelle strut (component D), the motor (component E), and the propeller (component F). The letter labels are provided for each component in the propeller mounting structure to aid in discussions later in this paper. The nacelle strut (component D) was rapid prototyped using stereolithography (SLA®) and housed a Medusa MR-012-030-4000 0.47 in. (12 mm) diameter 4000 kV brushless in-runner motor. The motor (component E) had a 0.059 in. (1.5 mm) shaft and the ability to test 2–5 in. (50.8–127 mm) diameter propellers (component F) without the need of a gearbox. The wires that powered the motor ran through the nacelle strut to a Castle Creations

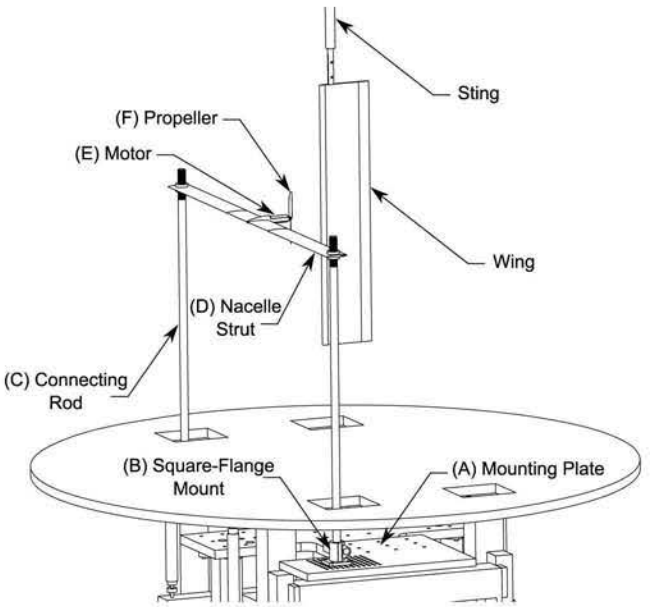

Fig. 2 Isometric view of the propeller mounting structure in tractor configuration in the tunnel test section (letter labels provided for each component as a reference aid).

Phoenix-10 speed controller connected to a BK Precision 3-15 V (40 A continuous) power supply. The nacelle strut was set horizontally in the tunnel test section using two connecting rods (component C) bolted onto mounting plates (component A) via square-flange mounts (component B). The plates were attached to the UIUC main platform balance, for which the center of rotation was aligned with that of the LRN-FB and the wing quarter-chord, giving the propeller the ability to match its angle of attack with that of the wing during angle-of-attack sweep runs. The propeller mounting structure could be placed in either a tractor or pusher configuration.

A PC with a National Instruments NI PCI-6052E data-acquisition (DAQ) board and LabVIEW software was used for communication with the wind-tunnel setup. The test section dynamic pressure was measured with a differential pressure transducer connected to static pressure ports in the wind-tunnel inlet and test section. The ambient temperature and pressure were measured with a thermocouple and transducer, respectively, located in the laboratory. Lift, drag, and moment data from the load cells in the LRN-FB were passed through signal conditioners to amplify and filter the signals for the DAQ board. Each run involved taking measurements of the wing for both increasing and decreasing angles of attack in succession to capture any possible aerodynamic hysteresis.

For the propeller mounting structure, control of the Medusa motor was done through the PC via a Vexa Controls servo exciter connected to the speed controller. During a run, the LabVIEW code adjusted the voltage sent to the servo exciter to achieve a prespecified propeller rotation rate. A red laser with a wavelength of 630–680 nm and a phototransistor with a rise time of 5 μs was used to measure the rotation rate of the propeller. The laser was placed outside the test section and directed to pass through the propeller disk area to the phototransistor located on the opposing side of the test section. The output from the phototransistor was amplified so that the maximum voltage, when the laser shined on the phototransistor, was over 2 V. When spinning, the propeller blades blocked the laser beam, and the output voltage dropped to around zero. The voltage from the system was measured at 40,000 Hz and capped at 2 V to produce a square wave. The rotation rate was calculated by dividing the number of voltage peaks by the sample time and by the number of propeller blades. The phototransistor rise time and the sample rate have been more than sufficient in finding the typical rotation rates for the propellers tested. Rotation rates found from this system have been compared to results from a handheld digital tachometer, and the results agreed.

During a run, the entire data-acquisition process was automated. The data were corrected for three-dimensional tunnel effects according to the methods outlined in [27]. Note that the corrections performed did not account for the propeller mounting structure. The relative uncertainties of the lift, drag, and moment coefficients were calculated to be 3.3, 2.7, and 4.6%, respectively, using the methods introduced by Kline and McClintock [28] and further discussed by Coleman and Steel [29]. Further details regarding uncertainty quantification of the LRN-FB can be found in Ref. [25].

B. Wing

All experiments were performed with a rectangular wing using the Wortmann FX 63-137 airfoil. The Wortmann wing had an aspect ratio $\mathcal{R}$ of four and was rapid prototyped using SLA to tolerances of approximately ± 0.005 in. (0.127 mm) [30], ensuring model accuracy and surface quality. The wing had a chord length c of 3.5 in. (88.9 mm) and a wingspan b of 14 in. (355.6 mm). A drawing of the Wortmann FX 63-137 airfoil is shown in Fig. 3. Its rotation axis was located on the quarter-chord of the airfoil. Given that the Wortmann wing was cambered, the rotation axis was located 0.17 in. (4.44 mm) above the chord line of the wing.

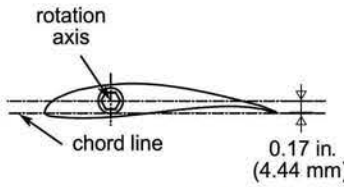

Fig. 3 Wortmann FX 63-137 airfoil with rotation axis on the airfoil quarter-chord.

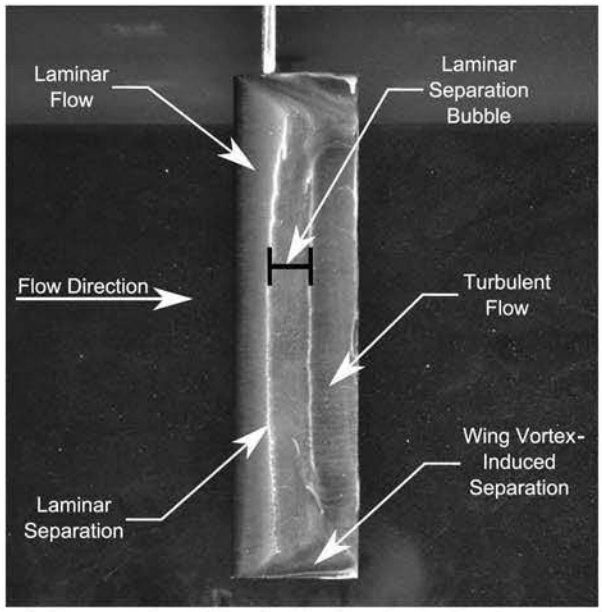

Fig. 4 Upper-surface oil flow visualization of major flow features on the Wortmann FX 63-137 rectangular wing with an $\mathcal{R}$ of four ($\alpha = 9$ deg, $Re = 90{,}000$) [26].

The Wortmann FX 63-137 airfoil was chosen because it was a high lift airfoil and had been widely tested in many wind-tunnel facilities. The Wortmann airfoil also exhibited characteristics inherent for low-Reynolds-number airfoils/wings operating close to the critical Reynolds number, such as laminar separation, the formation of the laminar separation bubble, prestall hysteresis, and poststall hysteresis. Some of these characteristics are evident in Fig. 4, which shows a photograph of fluorescent oil flow over the upper surface of the Wortmann wing at $\alpha = 9$ deg and $Re = 90{,}000$. The photograph clearly shows flow characteristics such as the laminar flow, laminar separation bubble, and turbulent flow regions. Wing vortex-induced separation is also observed in the region of the wingtips. This fluorescent oil flow visualization technique will also be employed to describe key flow features captured later in this paper. The technique involves first applying a smooth layer of matte black Ultracote Plus® on the upper and lower surfaces of the wing. A mixture of Tracer TP34000601 UV fluorescent leak detection die and standard mineral oil is then applied using an airbrush as a thin layer on the wing upper surface. The mineral oil used ensures that the dye mix has enough viscosity to be minimally affected by the influences of gravity. More details of the fluorescent oil flow visualization technique used can be found in Ref. [25].

C. Propellers

A total of 10 right-hand propellers ranging in diameter from 3 to 5 in. (76.2 to 127 mm) in both tractor and pusher configurations were tested. These propellers varied in diameter, blade planform, pitch, and number of blades to determine how differences in propeller geometry might affect the performance of the wing. The number of blades, the diameter, and the pitch for each propeller are listed in Table 1. The performance data for the propellers were gathered using a wind-tunnel testing rig designed to measure propeller thrust and torque. Information on the testing rig and the performance data for the propellers can be found in the works of Deters et al. [31,32] and Brandt [33]. The relative uncertainties of the C_T and C_P data were calculated to be 0.64 and 0.52%, respectively.

Typical propeller performance results are shown in Fig. 5 for the Grand Wing Servo-Tech Company (GWS) 5×4.3 propeller. The thrust coefficient C_T, power coefficient C_P, and efficiency η variation

Table 1 Propellers tested

Propeller name	Blades	Diameter	Pitch
GWS 5 × 4.3	2	5 in. (127 mm)	4.3 in. (109.2 mm)
GWS 4 × 4	2	4 in. (101.6 mm)	4 in. (101.6 mm)
GWS 3 × 3	2	3.2 in. (81.3 mm)	3 in. (76.2 mm)
NR640-5ab	2	5 in. (127 mm)	3.16 in. (80.3 mm)
NR640-5abc	3	5 in. (127 mm)	3.16 in. (80.3 mm)
NR640-5abcd	4	5 in. (127 mm)	3.16 in. (80.3 mm)
NR640-5ab + 5	2	5 in. (127 mm)	4.29 in. (109 mm)
DA4002-5ab	2	5 in. (127 mm)	3.75 in. (95.25 mm)
DA4002-5ab + 5	2	5 in. (127 mm)	4.92 in. (125 mm)
DA4052-5ab + 5	2	5 in. (127 mm)	4.92 in. (125 mm)

with the propeller advance ratio J are shown in Figs. 5a–5c. The Reynolds number is based on propeller dimensions and is defined by the chord and rotation speed at the 75% blade station. The windmill-brake state ($C_T < 0$) for the GWS 5 × 4.3 propeller was found from the C_T performance data (Fig. 5a) to start at an advance ratio J between 0.76 and 0.8. Note that, in the windmill-brake state, the flow behind the propeller was reduced (i.e., propeller was creating drag and not thrust).

D. Propeller-Induced Flow Conditions

All propellers were tested in both tractor and pusher configurations. The propellers were centered on the wing along the span (see Fig. 2) and located 0.17 mm above the wing chord with a zero incidence angle to the wing chord line. Measurements were taken with the origin located on the wing rotation axis (LRN-FB centerline) as shown in Figs. 6a and 6b. The X axis of the measurement system was defined as being parallel to the chord line of the wing with the origin at the rotation axis of the wing. The Z axis of the measurement system was perpendicular to the X axis of the wing. Propeller location measurements were normalized by the diameter of the propeller tested and measured from the wing leading edge for the tractor configuration (see Fig. 6a) or the trailing edge for the pusher configuration [see Fig. 6b]. To aid in the presentation of results later in the paper, the two different propeller locations tested are tabulated in Table 2. The $0.5D$ distance for the tractor configuration was chosen based on the contraction of the propeller slipstream as observed in Refs. [32,34]. By $0.5D$ downstream from a propeller,

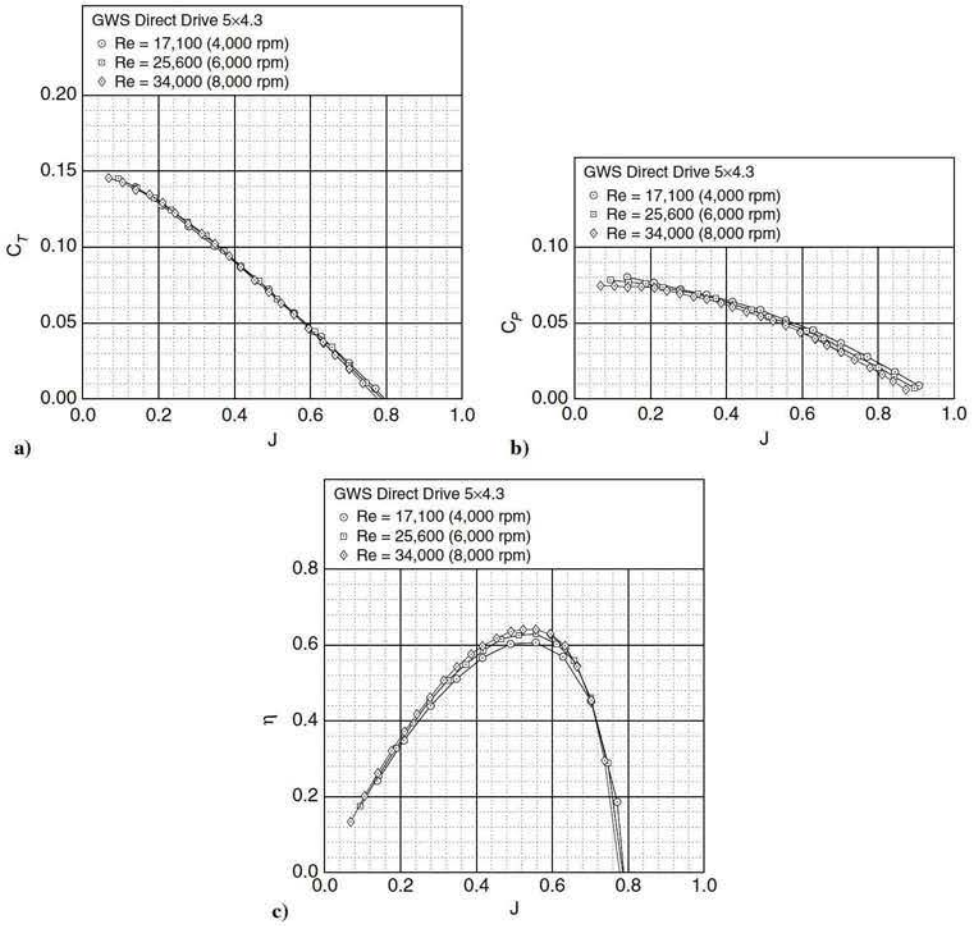

Fig. 5 GWS 5 × 4.3 performance data: a) thrust coefficient, b) power coefficient, and c) efficiency.

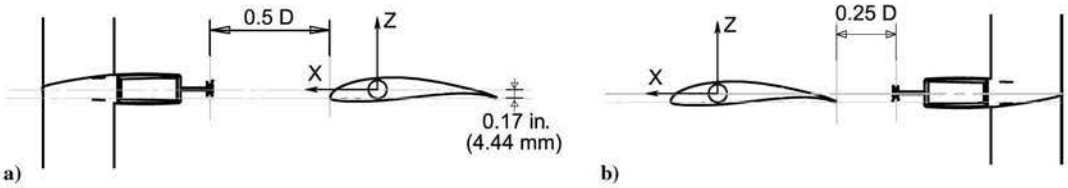

Fig. 6 Propeller positions tested: a) tractor ($0.5D$ from leading edge) and b) pusher ($-0.25D$ from trailing edge). Distances scaled based on a 5 in. (127 mm) propeller diameter.

Table 2 Propeller positions tested

Position name	*X* Location	*Z* Location
Tractor	0.5*D* from leading edge	0*D*
Pusher	−0.25*D* from trailing edge	0*D*

the slipstream has contracted and the diameter stays mostly constant further downstream. The pusher position of 0.25*D* was chosen due to positioning limitations associated with the propeller mounting structure.

III. Results and Discussion

This section details performance results obtained using the LRN-FB under various propeller–wing configurations. First, Sec. III.A provides the wing-only (no propeller mounting structure) performance and upper-surface flow visualization results for the Wortmann FX 63-137 wing. In the proceeding sections, these results will be labeled "clean." In Sec. III.B, the effect of the nacelle strut (components A–E of the propeller mounting structure) on wing performance is quantified both in tractor and pusher configurations. The aerodynamic performance results with only the nacelle strut will be labeled "strut only." Section III.C introduces results from propeller-induced flow experiments where the entire propeller mounting structure (components A–F) was included. Note that, for the purposes of clarity, all plots in this section, apart from those in Sec. III.A, have markers plotted at every other data point.

A. Wing Performance Without Propeller

Drag polars, lift curves, moment curves, and lift-to-drag ratio curves at varying Reynolds numbers for the Wortmann wing are shown in Figs. 7a, 7b, and 8 [25,35]. Data were taken from an angle of attack of −15 to 25 deg for increasing and then decreasing angles of attack to capture possible aerodynamic hysteresis. The results were taken using the LRN-FB with no propeller mounting structure.

The low $C_{L_{max}}$ seen in Fig. 7 for Reynolds numbers of 80,000 and below is a result of the laminar boundary layer separating and not reattaching onto the wing surface, thereby forming what can be termed as a long laminar separation bubble [36,37]. Initially, as the angle of attack increases, the airfoil follows a typical linear lift curve slope. In the midlift range, however, as the angle of attack increases, the drag increases dramatically with a concurrent flattening of the lift curve. The separated laminar boundary or shear layer has insufficient energy to form a short laminar separation bubble. A short laminar separation bubble forms when the separated laminar shear layer transitions to turbulent flow and reattaches to the wing. The flow downstream of the short separation bubble is then turbulent. The short laminar separation bubble forms between the Reynolds numbers of 80,000 and 90,000 for the Wortmann wing. The short bubble formation and consequent turbulent flow region results in the airfoil moving from a stalled state to being unstalled. An increase in lift and a reduction of drag are then observed, thereby leading to a jump in the lift-to-drag ratio as shown in Fig. 8 for a Reynolds number of 90,000 over the angle-of-attack range from 8 to 18 deg.

At a Reynolds number of 90,000, both prestall and poststall hysteresis loops are observed. Prestall hysteresis or long bubble hysteresis, as discussed in Refs. [37,38], is a type of lift hysteresis that is caused initially by the formation of a long laminar separation bubble with an increasing angle of attack. As the angle of attack further increases, the long bubble collapses to form a short laminar separation bubble over the wing. The short bubble formation yields a jump in the lift of the wing, a drop in drag, and a corresponding increase in the lift-to-drag ratio (see Fig. 8). The effect of bubble formation is also captured in the moment data (see Fig. 7). With decreasing angles of attack, however, the reformation of the long separation bubble occurs at a lower angle of attack as compared to its collapse, therefore creating a hysteresis loop. To date, as far as the authors are aware, prestall hysteresis has not been captured in the literature for FX 63-137 wings and has been rarely observed on airfoils [37,39,40]. Although repeatedly reproduced, prestall hysteresis only occurred at the Reynolds number of 90,000 that was tested for the Wortmann wing. No prestall hysteresis was observed at Reynolds numbers of 80,000 and 100,000.

Poststall hysteresis is observed and repeatedly reproduced at Reynolds numbers of 90,000 and 100,000. Poststall hysteresis occurs when the short laminar separation bubble on the wing upper surface bursts and flow separation occurs, resulting in a large loss of lift. As the angle of attack then decreases, the short laminar separation bubble reattaches at an angle of attack lower than that for which the burst occurred, thereby creating the hysteresis loop.

Results from Fig. 8 show that, at Reynolds numbers higher than 90,000, there exists a large angle-of-attack range ($\alpha = -1$ to 13 deg) for which high lift-to-drag ratios ($C_L/C_D > 7.5$) are achieved.

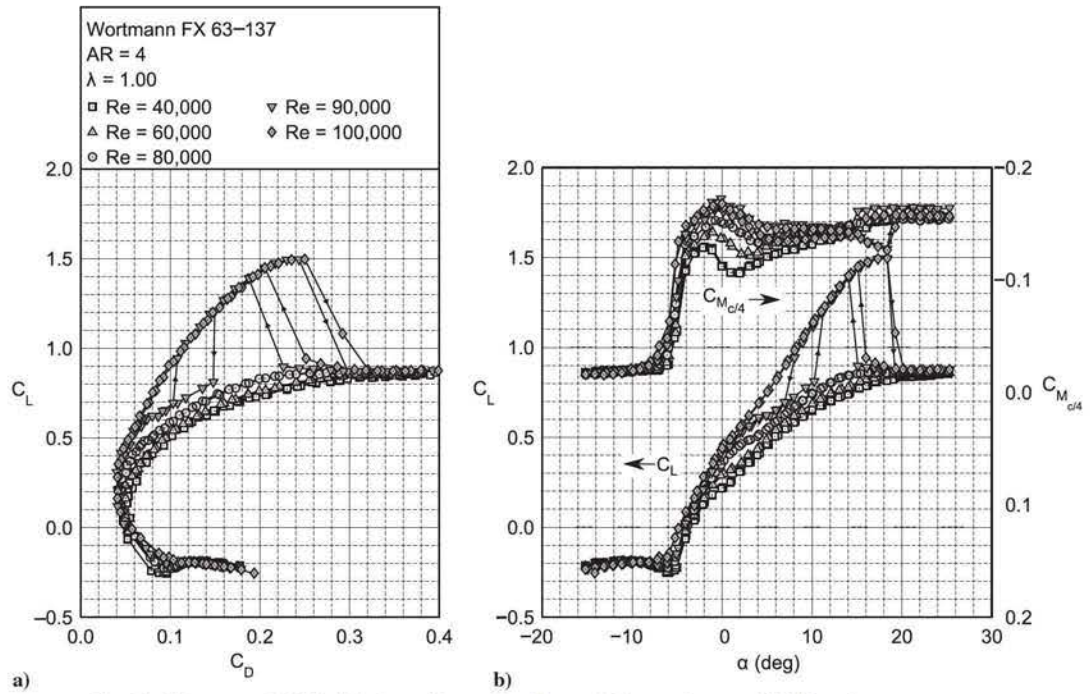

Fig. 7 Wortmann FX 63-137 wing with an $\mathcal{R}$ of four: a) drag polars, and b) lift and moment curves.

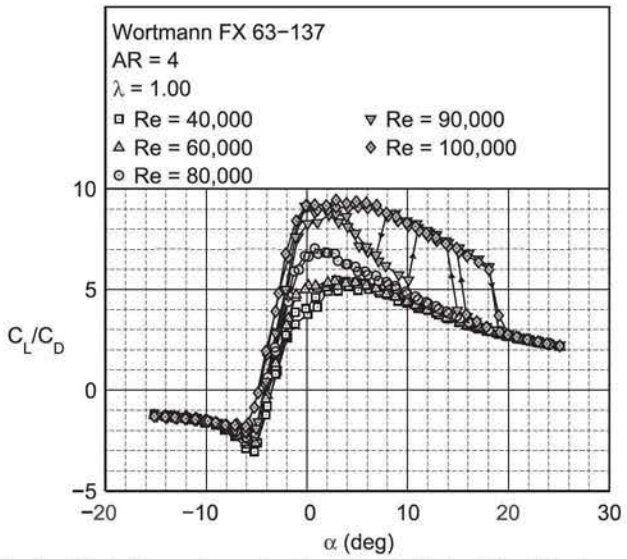

Fig. 8 Lift-to-drag ratio as a function of angle of attack for a Wortmann FX 63-137 wing with an $\mathcal{R}$ of four.

Another conclusion from the performance results is that the stall angle of attack is observed to increase with an increase in Reynolds number. Also, it is important to note the decrease in the zero-lift angle of attack (more negative) with increasing Reynolds number. This trend is similar to that discussed by Bastedo and Mueller [41].

Surface oil flow visualization was performed at a number of angles of attack to further understand the interesting flow phenomena on the Wortmann wing at a Reynolds number of 90,000. Figures 9a–9h show photographs of the upper surface of the Wortmann wing at these different angles of attack. Laminar flow accompanied by a flow separation or a long separation bubble is seen at angles of attack of −2 and 7 deg. The bubble moves toward the leading edge of the wing with an increasing angle of attack. For both of these angles of attack, it can also be observed that the turbulent flow has not fully developed over the aft section of the wing. At an angle of attack of 9 deg, the long bubble "collapses" into a short separation bubble. Fully developed turbulent flow is also seen at the trailing edge of the wing. It can be concluded that, because the short separation bubble forms, the jump in the lift for the wing has prematurely occurred, and the prestall hysteresis stage (seen in Figs. 7 and 8 for $Re = 90,000$) is bypassed. Given that prestall hysteresis is repeatedly captured both before and after surface oil flow visualization tests are performed, it is posited

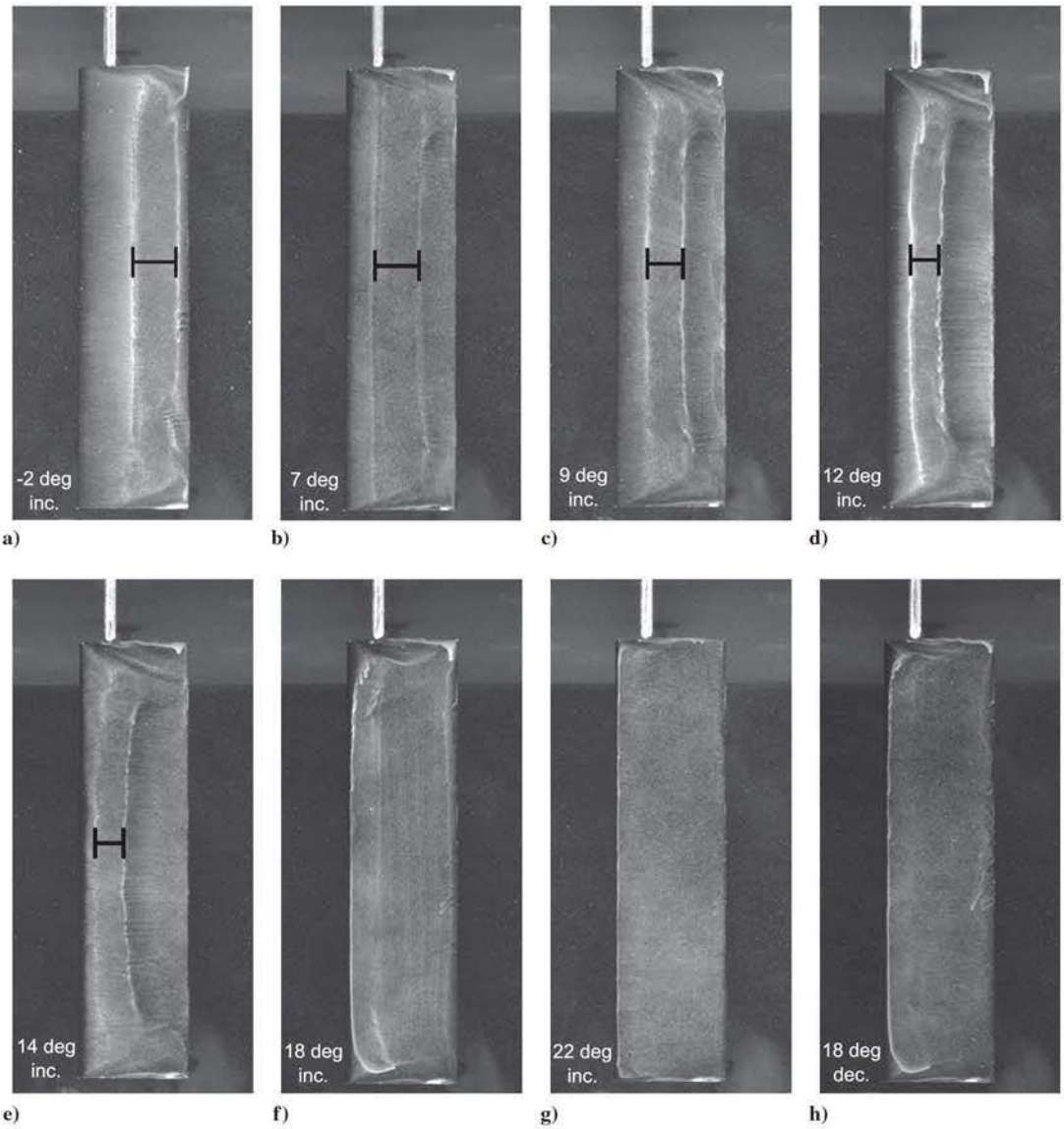

Fig. 9 Upper-surface oil flow visualization showing major flow features on the Wortmann FX 63-137 wing with $\mathcal{R} = 4$ at $Re = 90,000$, showing α value with a–g) increasing (inc.) α and h) decreasing (dec.) α.

that the thickness and skin-friction changes on the upper surface of the wing due to the use of Ultracote Plus and the fluorescent oil may have affected the conditions necessary for prestall hysteresis to occur.

The short separation bubble is seen to further move toward the leading edge and reduce in length at an angle of attack of 12 deg. A small laminar flow region is seen at an angle of attack of 14 deg, with the separation bubble and turbulent regions covering most of the upper surface of the wing. From an angle of attack of −2 to 14 deg, a steady growth is observed in the disturbance caused by the wingtip vortices that is likely caused by its vortex strength increase with lift. At an angle of attack of 18 deg, the bubble is not present, and the bands of oil on the upper surface of the wing represent the fully turbulent region of the flow over the wing. Finally, at an angle of attack of 22 deg, the unaltered oil flow indicates complete flow separation from the upper surface of the wing. Poststall hysteresis is captured when the angle of attack of the wing is initially set to 22 deg and then reduced to 18 deg during a flow visualization test run. Figure 9h shows that the flow is still fully separated in comparison with the fully turbulent flow in Fig. 9f.

B. Effect of Nacelle Strut

Before presenting the effects of propeller-induced flow on the aerodynamic performance of wings, the effects of the nacelle strut [components A–E (see Fig. 2) of the propeller mounting structure; no propeller] on the aerodynamics of the wing are presented. A comparison was performed on the Wortmann wing results for a clean configuration case, the nacelle strut in the tractor configuration case [strut only (T)], and the nacelle strut in the pusher configuration case [strut only (P)]. Drag polars are presented in Figs. 10a–10d for the Reynolds numbers of 60,000 to 90,000 to chart the difference between the three configurations. Note that the strut-only comparisons made here are for the nacelle strut that is located based on a propeller diameter of 5 in. (127 mm). The performance results will differ slightly from the strut-only results for a nacelle strut located for a 3.2 in. (81.3 mm) propeller.

The results in Figs. 10a–10d show that the nacelle strut in the tractor configuration [strut only (T)] influences the aerodynamic properties of the wing at Reynolds numbers close to when the separation bubble forms on the Wortmann wing. In addition, the

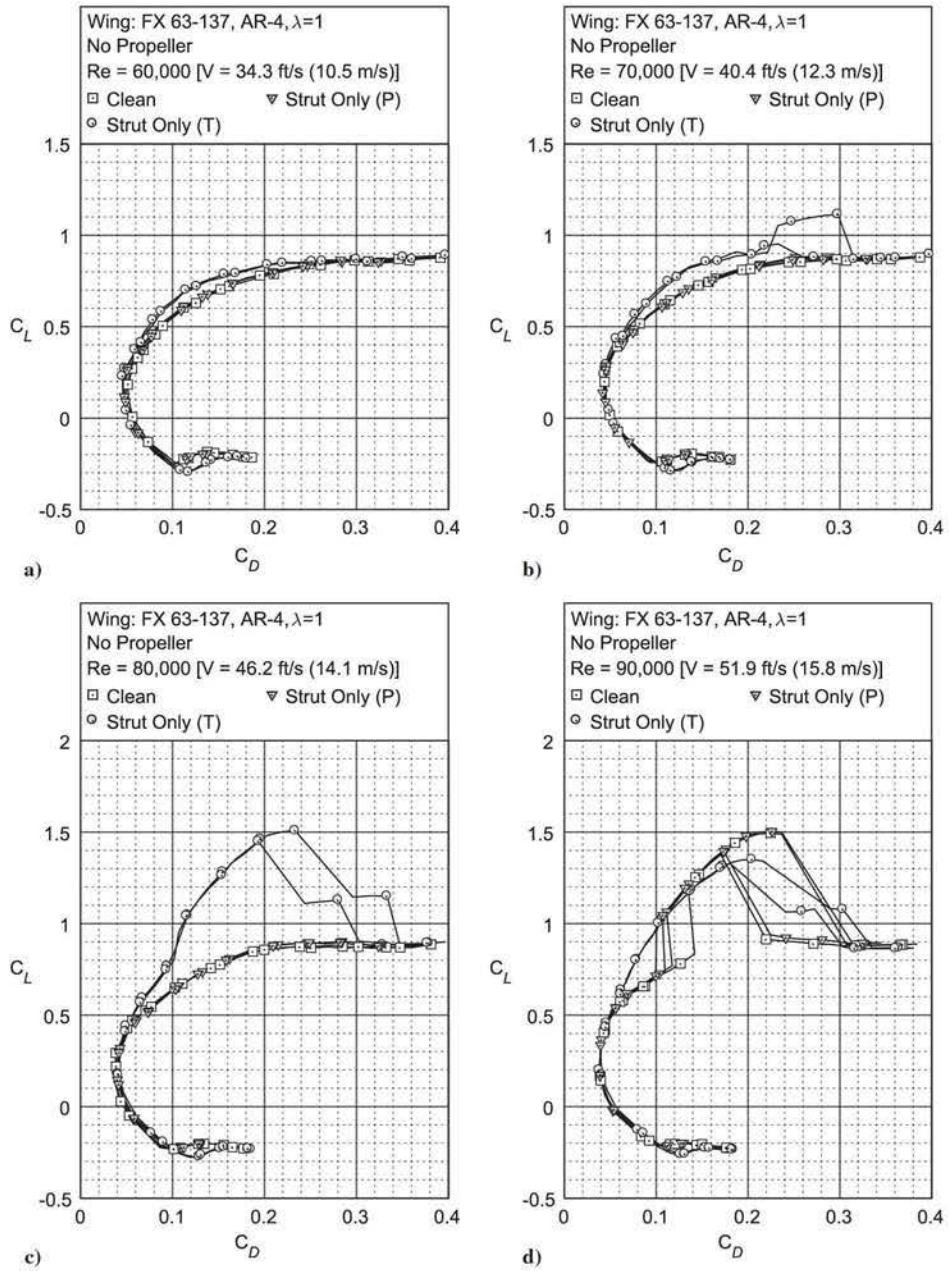

Fig. 10 Wortmann FX 63-137 $AR = 4$ rectangular wing drag polars comparing clean, nacelle strut in tractor configuration and nacelle strut in pusher configuration cases at different Reynolds numbers of a) 60,000, b) 70,000, c) 80,000, and d) 90,000.

effect of the strut only (T) configuration on the flow over the upper surface of the Wortmann wing can also be observed from surface oil flow visualization tests performed as shown in Figs. 11a and 11b.

At a Reynolds number of 60,000, Fig. 11a shows a minimal effect of the nacelle strut on the laminar separation line of the wing. The flow visualization results corroborate the drag polar results shown in Fig. 10a, where small differences are observed in the drag polar results between the clean and strut only (T) cases. Figure 11b, however, shows a region of turbulent flow that is roughly the width of the motor mount of the nacelle strut and a separation bubble over the

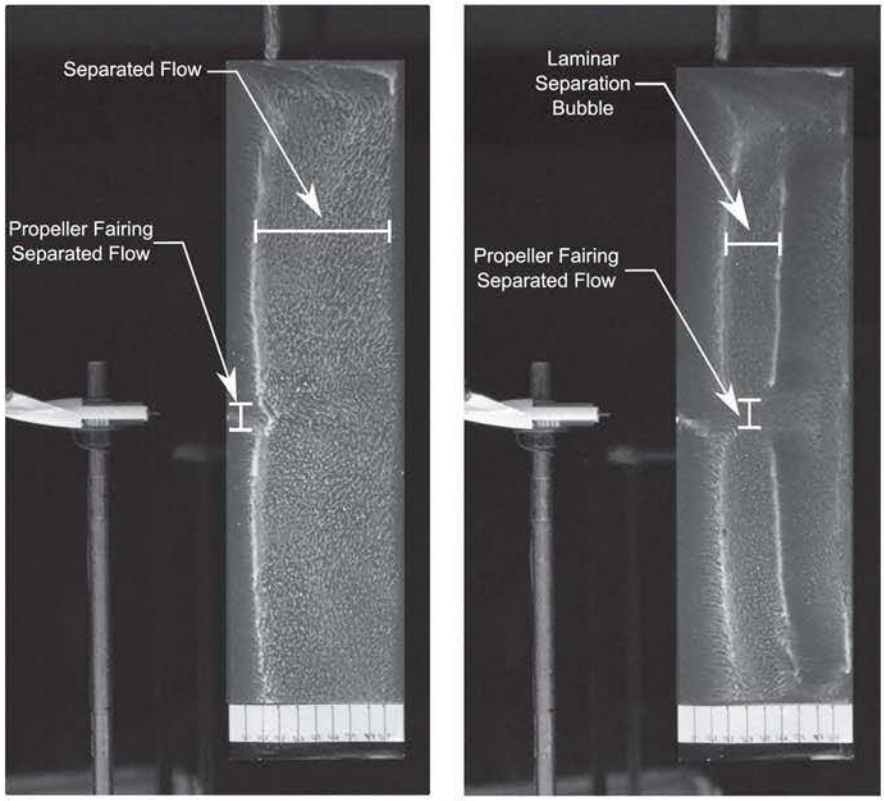

Fig. 11 Upper-surface oil flow visualization results of the Wortmann FX 63-137 $AR = 4$ rectangular wing with nacelle strut in tractor configuration (no propeller) at angle of attack of 9 deg: a) $Re = 60{,}000$ and b) $Re = 80{,}000$.

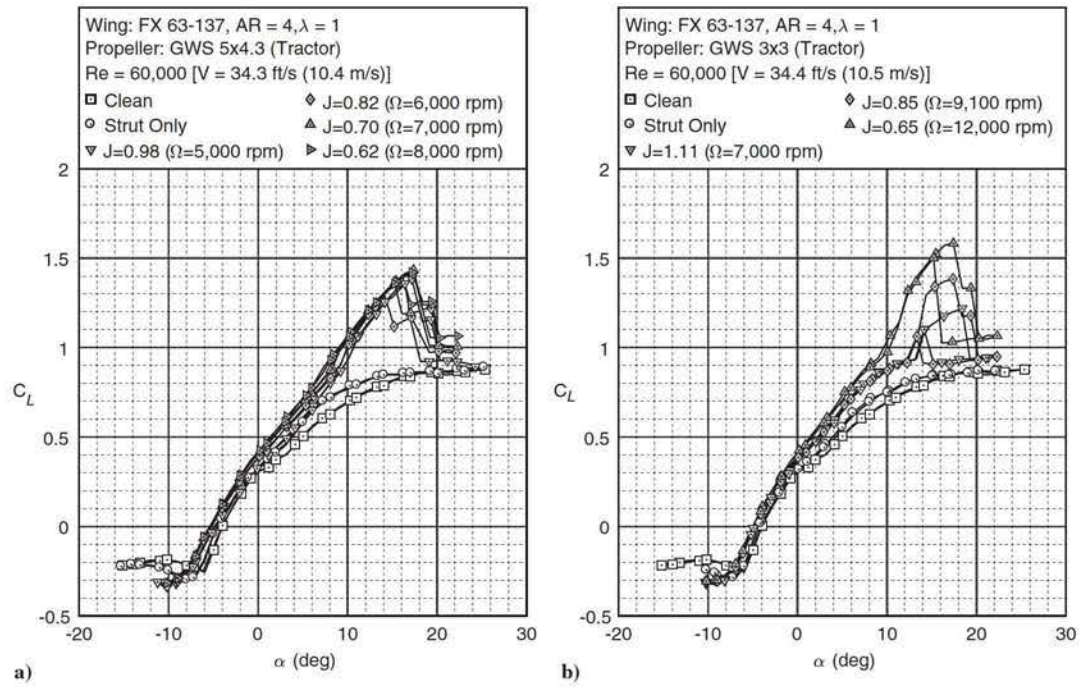

Fig. 12 Effect of increasing propeller advance ratio on lift curve of the Wortmann FX 63-137 $AR = 4$ rectangular wing at a Reynolds number of 60,000 for GWS a) 5×4.3 and b) 3×3 propellers.

rest of the wing at a Reynolds number of 80,000. The performance data in Fig. 10c show that the turbulent flow and separation bubble region are caused by the strut only (T) configuration. From these observations, it can be concluded that the effect of the strut only (T) configuration is such that the separated flow from the setup induces the formation of a separation bubble on the Wortmann wing at lower Reynolds numbers than that of the clean or pusher configuration. Note that these effects will change once a rotating propeller is introduced and located between the strut and the wing. In the pusher configuration [strut only (P)], the nacelle strut is located aft of the wing, so the minimal effects observed between the clean and strut only (P) performance data in Fig. 10a–10d may be attributed to wind-tunnel blockage effects.

C. Propeller-Induced Flow Experiments

All propeller-induced flow experiments were conducted between the wing chord Reynolds numbers of 60,000 to 90,000. A maximum Reynolds number of 90,000 was chosen because that was the Reynolds number at which the propellers were in a brake state (negative C_T) at the maximum propeller rotation rates Ω tested. The most significant effects were observed in the lift and drag curves of the Wortmann wing. These effects will be discussed in the following subsections.

1. *Effect of Propeller Advance Ratio: Tractor Configuration*

The lift, drag, and lift-to-drag ratio curves as a function of angle of attack for the Wortmann wing and propeller in the tractor configuration are shown for a wing chord Reynolds number of 60,000 in Figs. 12–14. The advance ratio sweeps performed are shown specifically for the GWS 5×4.3 and GWS 3×3 propellers. As noted in Table 1, the GWS 5×4.3 is a two-bladed propeller with a diameter of 5 in. (127 mm) and a pitch of 4.3 in. (109.2 mm). Correspondingly, the GWS 3×3 propeller is a two-bladed propeller with a diameter of 3.2 in. (81.3 mm) and a pitch of 3 in. (76.2 mm). To aid in the discussion, the rotation rates, the corresponding advance ratios, and the corresponding induced velocities for both propellers are tabulated in Table 3. The induced velocities presented are calculated using momentum theory from available propeller C_T data taken in Refs. [31,32]. Induced velocities left blank in Table 3 mean that no C_T data are measured at those conditions. The choice of rotation rates tested is based on the availability of propeller performance data and the capabilities of the motor. In addition, another goal is to include rotation rates for which zero or negative induced flow velocities are produced.

The clean and strut-only lift (Fig. 12), drag (Fig. 13), and lift-to-drag ratio (Fig. 14) curves show performance results indicative of a long

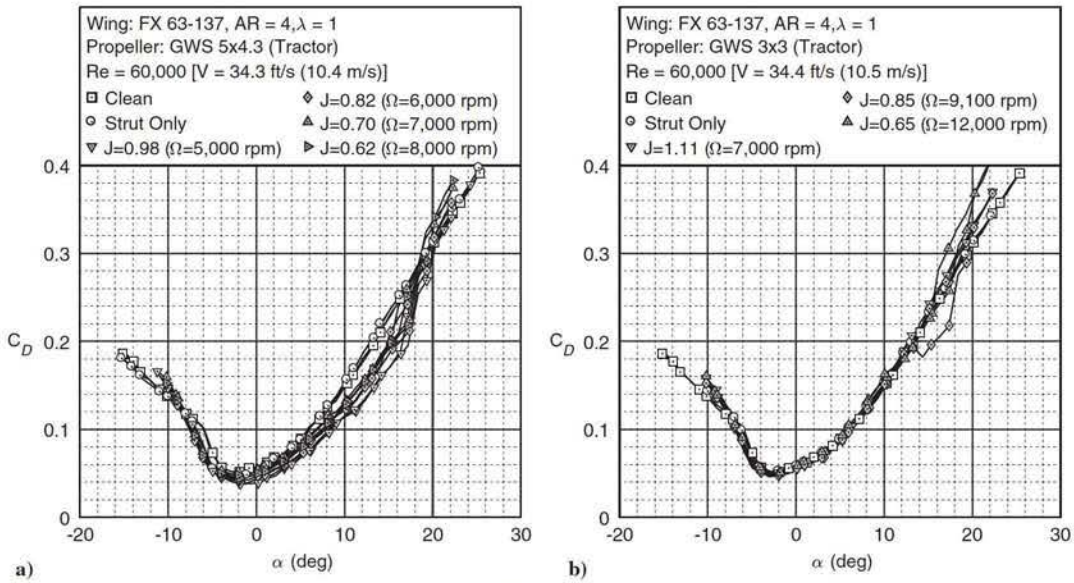

Fig. 13 Effect of increasing propeller advance ratio on drag curve of Wortmann FX 63-137 $\mathcal{AR} = 4$ rectangular wing at a Reynolds number of 60,000 for GWS a) 5×4.3 and b) 3×3 propellers.

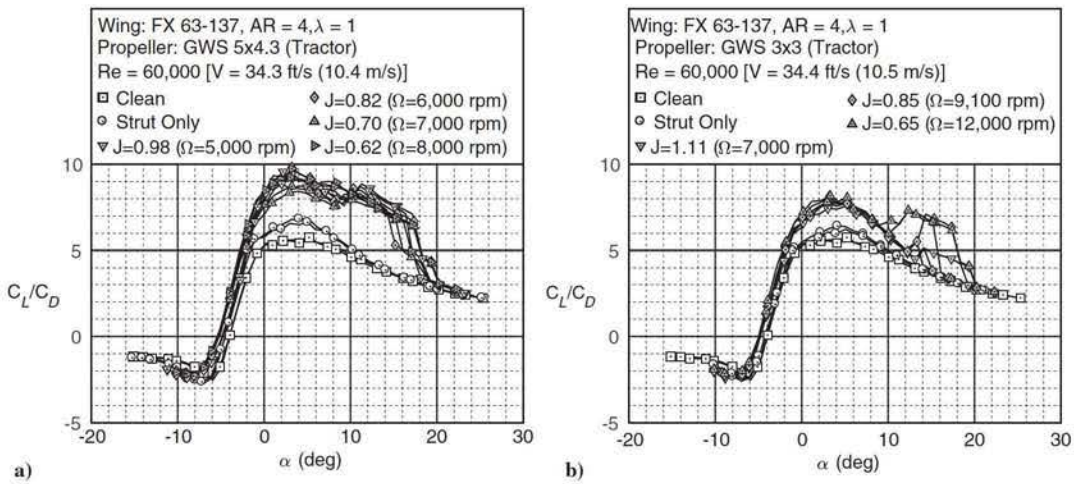

Fig. 14 Effect of increasing propeller advance ratio on lift-to-drag ratio curve of Wortmann FX 63-137 $\mathcal{AR} = 4$ rectangular wing at a Reynolds number of 60,000 for GWS a) 5×4.3 and b) 3×3 propellers.

Table 3 Propeller-induced velocities at $V_\infty = 34.4$ ft/s (10.5 m/s)

	GWS 5 × 4.3				GWS 3 × 3		
Ω, rpm	5,000	6,000	7,000	8,000	7,000	9,000	12,000
J	0.98	0.82	0.70	0.62	— —	0.86	0.65
w, ft/s	— —	−0.24	1.61	2.32	— —	0.78	4.01
w, m/s	— —	−0.07	0.49	0.71	— —	0.24	1.22

laminar separation bubble, as discussed in prior sections. For the propeller-on conditions ($\Omega > 0$), however, significant effects in lift and drag are observed for both propellers (GWS 5 × 4.3 and GWS 3 × 3). The lift curves show large increases in $C_{L_{max}}$ with the decreasing propeller advance ratio. An increase in the lift curve slope, mentioned in Refs. [16,17], is also observed. The GWS 5 × 4.3 propeller results (Fig. 12a) immediately show a jump in lift for all propeller-on conditions. Interestingly, for the GWS 3 × 3 case (Fig. 12b), the lift curve initially has characteristics indicative of a long laminar separation bubble (at $\alpha \leq 10$ deg). As the angle of attack increases further, a jump in lift occurs, suggesting the formation of a short separation bubble on the wing. The amount of lift increase and the angle of attack at which it occurs depend on the advance ratio of the propeller. Higher $C_{L_{max}}$ values are observed for the maximum rotation rate [$J = 0.65$, $w = 4.01$ ft/s (1.22 m/s)] case for the GWS 3 × 3 propeller as compared to the GWS 5 × 4.3 results and can be attributed to the increased dynamic pressure and local angle-of-attack changes caused by the higher induced velocities over the center portion of the wing. In addition, the size of the hysteresis loop decreases at lower advance ratios. Stall occurs from the bursting of the bubble, and the lift performance of the wing drops close to the stalled clean and strut-only wing performance results. The key thing to note here is that, for both propellers (primarily GWS 5 × 4.3), despite the low or even negative induced velocities produced (see Table 3), a substantial increase in lift is observed from the clean configuration.

Drag results for the GWS 5 × 4.3 propeller (Fig. 13a) show a pronounced reduction in drag at most angles of attack (−2 to 18 deg) with a decreasing advance ratio. A similar magnitude reduction in drag is not observed for the GWS 3 × 3 propeller (Fig. 13b). These observations are further reinforced by the C_L/C_D curves presented in Figs. 14a and 14b. The GWS 5 × 4.3 results (Fig. 14a) show a significant increase in the lift-to-drag ratio (a maximum of 70% increase is observed as compared with the clean configuration) at most angles of attack before stall. A smaller increase in lift-to-drag ratio is observed for the GWS 3 × 3 propeller case (Fig. 14b). Only at high angles of attack is there a jump in lift-to-drag ratio observed, corresponding the jump in lift shown in Fig. 12b.

Upper-surface oil flow visualization results (Figs. 15a–15c) are used to show the effects of the GWS 5 × 4.3 propeller on the flow over the Wortmann wing at a Reynolds number of 60,000. Figure 15a shows the Wortmann wing in the strut-only configuration at an angle of attack of 9 deg. Laminar flow separation and no reattachment (long laminar separation bubble) are observed on the wing at the 15–20% chord location based on the oil accumulation lines. At the same angle of attack (9 deg), the slipstream from the GWS 5 × 4.3 propeller rotating at 7000 rpm ($J = 0.7$) in the tractor configuration (Fig. 15b) creates a region of turbulent flow roughly the size of the propeller [5 in. (127 mm)] on the upper surface of the wing. In addition, the slipstream also induces the formation of a laminar separation bubble between 30 and 65% chord in the regions outside the propeller slipstream. As the angle of attack increases to 14 deg (Fig. 15c), the turbulent slipstream region is maintained but the separation bubble moves toward the leading edge of the wing and shortens.

To further understand the effects of the propeller slipstream in inducing turbulent flow over the Wortmann wing, experiments were performed where trips that were the span of the GWS 5 × 4.3 [5 in. (127 mm)] and GWS 3 × 3 [3.2 in. (81.3 mm)] propellers were placed on the Wortmann wing. A diagram of the trips on the wing for the 5 in. (127 mm) trip case is shown in Fig. 16. Based on surface oil flow visualization results, the trip tape was placed with its aft edge located at the 10% chord length to ensure that the trip induced turbulent flow ahead of when laminar boundary-layer separation occurred. The trips used were "plain trips" with dimensions of 0.125 in. (3.175 mm) in width and either 0.009 in. (0.229 mm) or 0.0135 in. (0.343 mm) in thickness. The lift-to-drag ratio (C_L/C_D) curves of the Wortmann wing in the different configurations are presented for the Reynolds

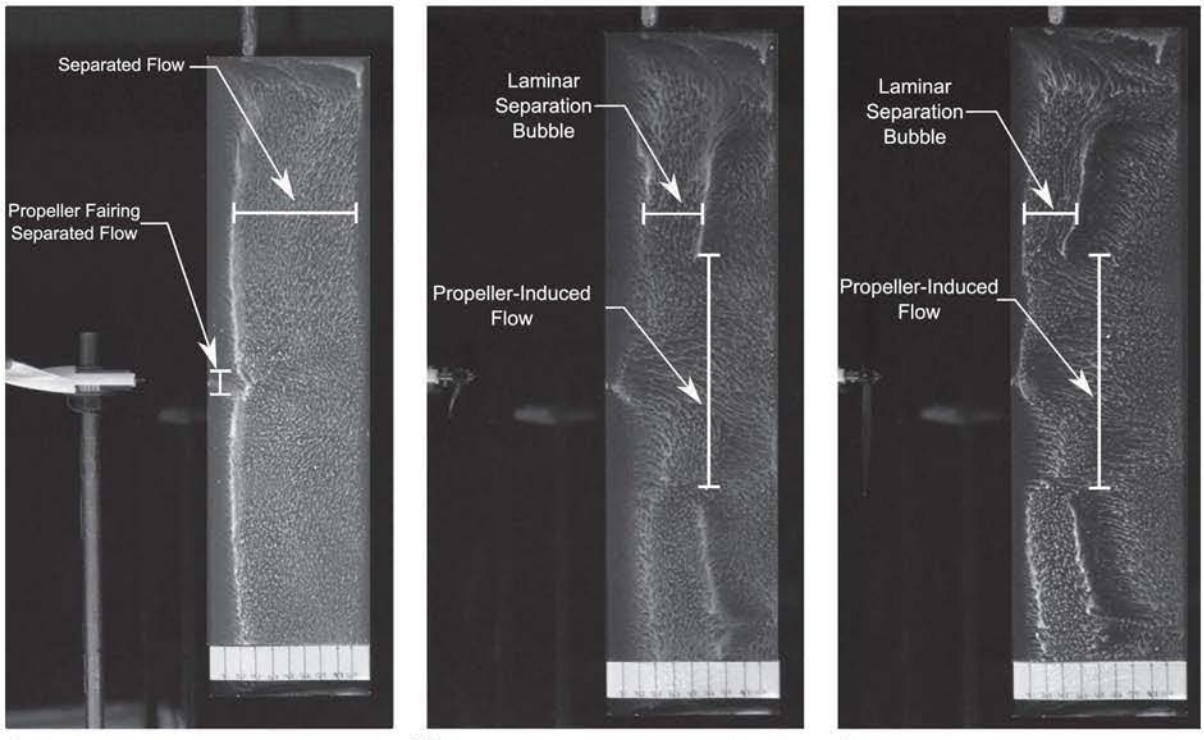

a) b) c)

Fig. 15 Upper-surface oil flow visualization results of the Wortmann wing at $Re = 90{,}000$ with strut only at a) $\alpha = 9$ deg, GWS 5 × 4.3 (tractor, $\omega = 7000$ rpm) at b) $\alpha = 9$ deg, and c) $\alpha = 14$ deg.

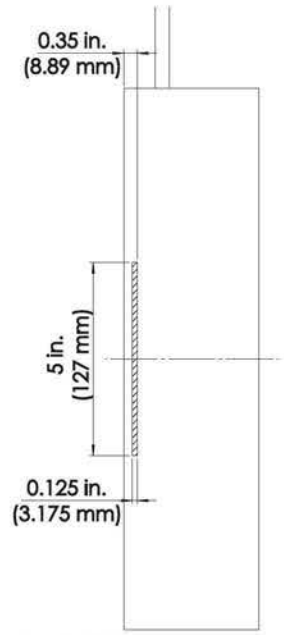

Fig. 16 Wortmann FX 63-137 $\mathcal{AR} = 4$ rectangular wing with 0.009-in.-thick (0.229 mm thick) or 0.0135-in.-thick (0.343 mm thick) trip tape with aft edge located at 10% chord [0.35 in. (8.89 mm)].

numbers of 60,000 in Figs. 17a and 17b. In addition, the percentage change Δ in $C_{L_{\max}}$ and $(C_L/C_D)_{\max}$ from the clean wing configuration results for the tests shown in Figs. 17a and 17b are tabulated in Table 4.

As discussed previously, the strut-only configuration affects the aerodynamics of the wing. Negligible effects are observed in $C_{L_{\max}}$, but slight increases are seen in $(C_L/C_D)_{\max}$ (see Table 4); as for this case, the short laminar separation bubble has not formed (see Fig. 17). It can also be observed from Fig. 17a that the GWS 5×4.3 propeller-on configuration augments the lift-to-drag ratio of the wing at all angles of attack. However, the trips [0.009 in. (0.229 mm) and 0.0135 in. (0.343 mm) thick] show smaller C_L/C_D augmenting effects at low angles of attack ($\alpha \leq 11$ deg). The GWS 3×3 propeller and trip case [Fig. 17b] are observed to provide a similar change in C_L/C_D at low angles of attack. However, no lift-to-drag ratio jump at high angles of attack is observed here. Also, from Table 4, the magnitude of augmentation in the lift-to-drag ratio obtained for the 5 in. (127 mm) propeller is higher in comparison with the 3.2 in. (81.3 mm) propeller, despite higher $C_{L_{\max}}$ values being reached by the GWS 3×3 propeller.

Observations made from the tractor configuration, oil surface flow visualization, and trip tests conducted have led to a key novel finding. Typically from the literature, two direct effects are attributed to propeller-on effects on wing performance, an increase in dynamic pressure, and a change in the local angle of attack along the wing (especially at high angles of attack), thereby causing separation delay and higher $C_{L_{\max}}$ values. For the low Ω cases tested where induced flow velocities are low or negative, no increased dynamic pressure is observed. In addition, given that the incidence angle between the propeller and wing is fixed at 0 deg, at the low angles of attack tested (-5 to 5 deg), the effects of a propeller in affecting the local angle of attack on the wing are minimal (swirl effects cancel out for a centered propeller). Despite the removal of these two key effects, significant augmentations in the lift-to-drag ratio are observed (up to a 70% increase from the clean configuration). It therefore can be concluded that the effect of a propeller in the tractor configuration is significant at low Reynolds numbers. The induced flow due to the propeller induces transition to turbulent flow over the center of the wing (see flow visualization results in Fig. 15). The propeller slipstream also induces the formation of a short laminar separation bubble outside this region, thereby contributing toward the significant augmentation of the lift-to-drag ratio, most importantly at low angles of attack. The reduction in observed drag is from the pressure (form) drag reduction of going from a long laminar separation bubble to a short laminar separation bubble. In addition, it has to be noted that the mechanism can be highly dependent on the advance ratio, the number of blades, and the diameter because transition is promoted by the helicoidal propeller wake passing over the wing surface. The lift-to-drag ratio augmentation effect seems to also be strongly dependent on the ratio of the propeller diameter to the wingspan. As the advance ratio decreases (increased induced flow velocities) for the propellers, the additional lift-to-drag and lift augmentations observed can be attributed to the effects of increased dynamic pressure and the change in the local angle of attack.

2. *Effect of Propeller Advance Ratio: Pusher Configuration*

Similar to the tractor configuration case, the lift, drag, and lift-to-drag ratio curves as a function of angle of attack for the Wortmann wing and the propeller in the pusher configuration are shown for a Reynolds number of 60,000 and varying propeller advance ratios in Figs. 18–20. It is evident from Figs. 18a and 18b that the propeller in a pusher configuration exhibits different aerodynamic performance characteristics for the Wortmann wing in comparison with the propeller in a tractor configuration. As Catalano [17] stated, the effect of the propeller-induced flow in the pusher configuration is to delay separation by moving the laminar separation point further aft on the wing.

At high advance ratios (low rotation rates) for both the GWS 5×4.3 and GWS 3×3 propellers, the lift curves (Figs. 18a and 18b) exhibit long laminar separation bubble characteristics but with increasing lift at high angles of attack. The increasing lift observed is most likely due to an increase in local flow velocity (dynamic pressure) and change in the local angle of attack of the wing in the

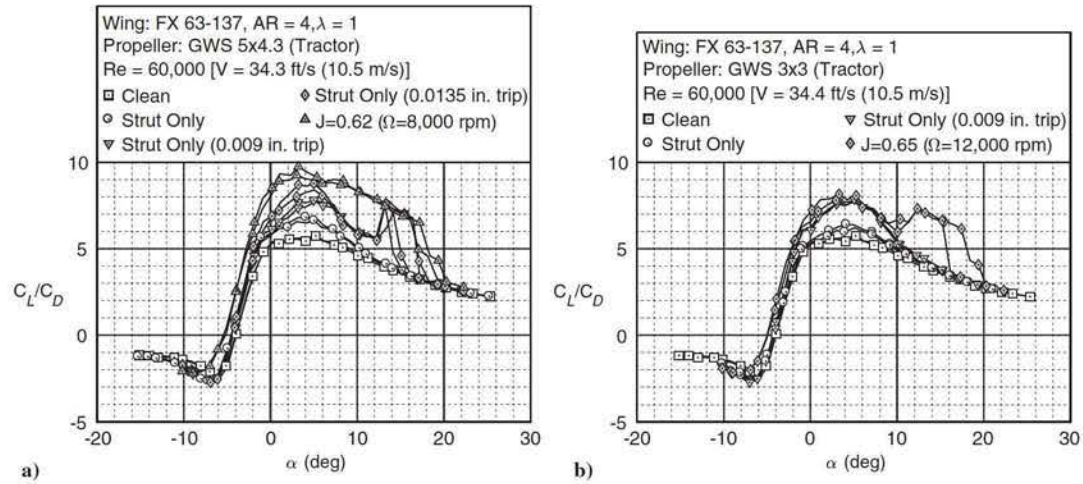

Fig. 17 Effect of the propeller advance ratio and trips on the Wortmann FX 63-137 $\mathcal{AR} = 4$ rectangular wing lift-to-drag ratio curve at a Reynolds number of 60,000: a) GWS 5×4.3 and b) GWS 3×3.

Table 4 Percentage change in wing performance

Configuration	$\Delta C_{L_{max}}$, %	$\Delta(C_L/C_D)_{max}$, %
GWS 5 × 4.3 (*tractor*)		
Clean	— —	— —
Strut only	1.5	18.5
Strut only (0.009 in. trip)	64.8	35.8
Strut only (0.0135 in. trip)	61.6	52.6
$J = 0.62$ (8,000 rpm)	61.9	69.4
GWS 3 × 3 (*tractor*)		
Clean	— —	— —
Strut only	−0.7	11.5
Strut only (0.009 in. trip)	1.9	37.0
$J = 0.41$ (12,000 rpm)	80.5	42.1

induced flow region, thereby causing longer regions of laminar flow and delayed separation. Similar effects were also observed from pusher performance results and flow visualizations taken on a Wortmann FX 63-137 wing tested by Catalano [17] at a Reynolds number of 450,000.

At low advanced ratios ($J = 0.70$ and $J = 0.61$ for GWS 5 × 4.3; $J = 0.68$ for GWS 3 × 3) and at angles of attack from 12 to 18 deg, wing performance results indicate the formation of a short separation bubble [jump in lift (Fig. 18); drop in drag (Fig. 19); jump in lift-to-drag ratio (Fig. 20)]. The delayed formation of the short separation bubble compared with the tractor configuration can be explained by the fact that the propeller is not inducing turbulent flow over the wing. Instead, only the local flow speed (dynamic pressure) is increased and the local angle of attack over the wing is affected. Therefore, the augmentation

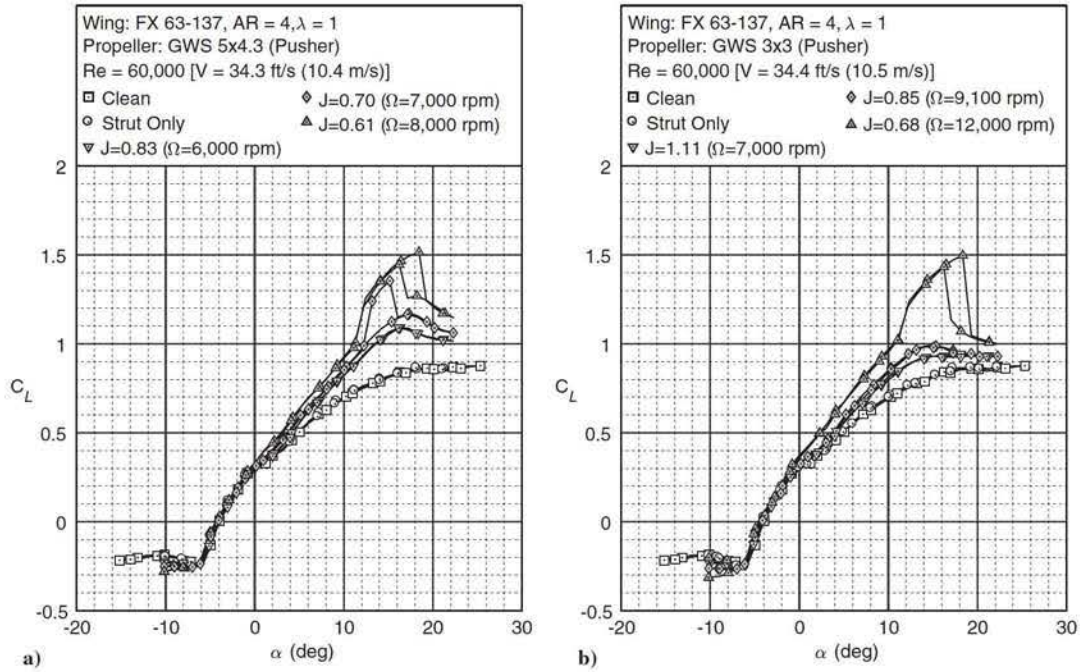

Fig. 18 Effect of increasing propeller advance ratio on lift curve of Wortmann FX 63-137 $AR = 4$ rectangular wing at a Reynolds number of 60,000 for GWS a) 5 × 4.3 and b) 3 × 3 propellers.

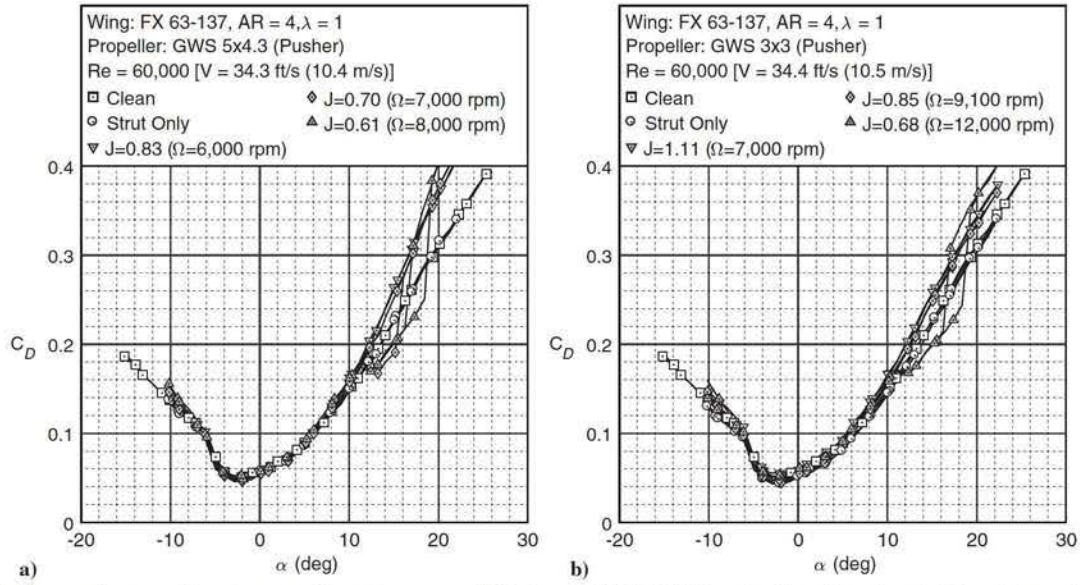

Fig. 19 Effect of increasing propeller advance ratio on drag curve of Wortmann FX 63-137 $AR = 4$ rectangular wing at a Reynolds number of 60,000 for GWS a) 5 × 4.3 and b) 3 × 3 propellers.

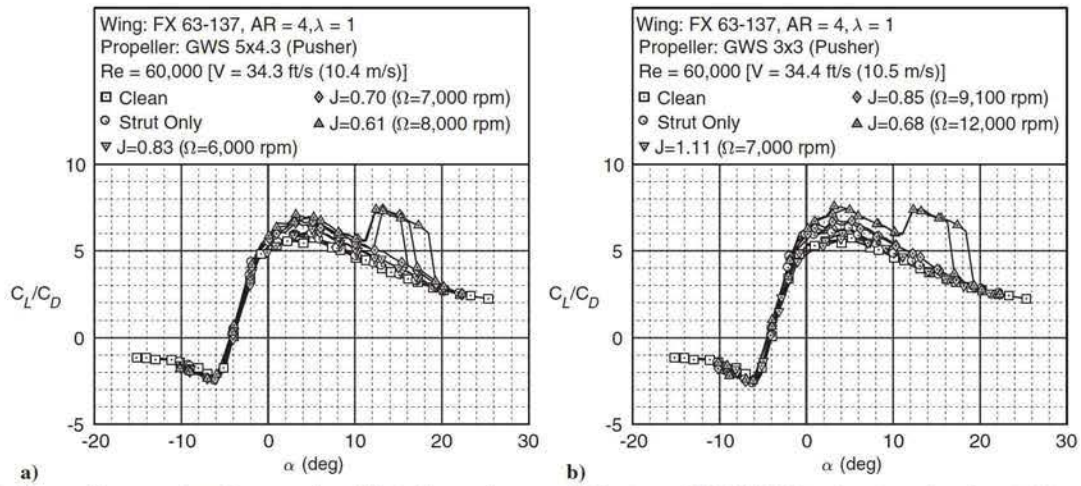

Fig. 20 Effect of increasing propeller advance ratio on lift-to-drag ratio curve of Wortmann FX 63-137 $AR = 4$ rectangular wing at a Reynolds number of 60,000 for GWS a) 5×4.3 and b) 3×3 propellers.

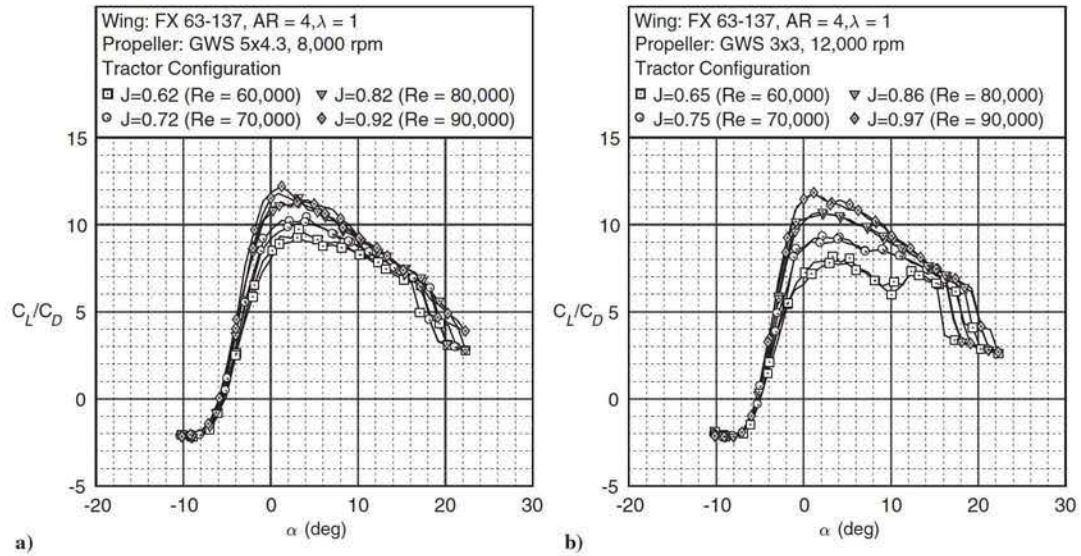

Fig. 21 Varying Reynolds number effects of Wortmann wing with GWS a) 5×4.3 at 8000 rpm and b) 3×3 propellers at 12,000 rpm in the tractor configuration.

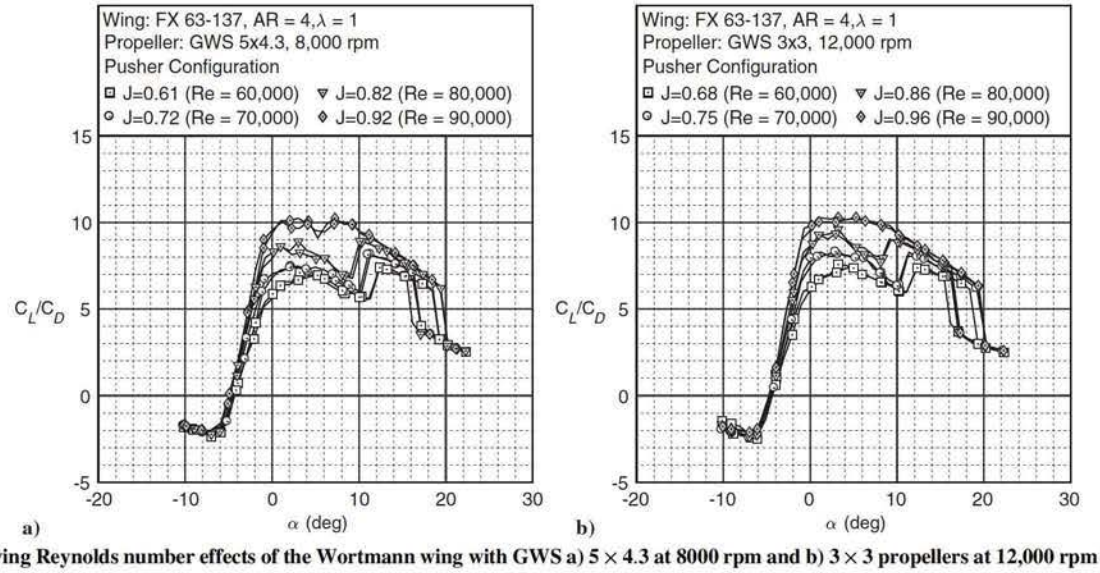

Fig. 22 Varying Reynolds number effects of the Wortmann wing with GWS a) 5×4.3 at 8000 rpm and b) 3×3 propellers at 12,000 rpm in the pusher configuration.

Table 5 Percentage increase in $C_L/C_{D_{max}}$ from clean configuration

	Reynolds number			
	60,000	70,000	80,000	90,000
	GWS 5 × 4.3			
J	0.62	0.72	0.82	0.92
Tractor (8,000 rpm), %	69.4	52.8	37.1	26.4
Pusher (8,000 rpm), %	23.5	9.7	1.8	6.2
	GWS 3 × 3			
J	0.41	0.48	0.55	0.62
Tractor (12,000 rpm), %	41.9	36.8	25.7	22.7
Pusher (12,000 rpm), %	31.5	21.9	13.9	6.6

of the lift-to-drag ratio observed in the tractor configuration results for low angles of attack is not evident for the pusher configuration results (see Figs. 20a and 20b). At higher angles of attack and low advance ratios, however, the movement of the laminar separation point toward the leading edge with increasing angles of attack and the increased local flow velocity allow for the flow to transition and reattach on the wing to form a short laminar separation bubble, thereby augmenting the lift-to-drag ratios to match those in the tractor configuration. From the aerodynamic performance results, the propeller diameter–to-wingspan ratio is significant in affecting the flow over the wing. A jump in lift-to-drag ratio is only observed in the case of an advance ratio of 0.68 for the GWS 3 × 3 propeller (Fig. 20b); whereas for the GWS 5 × 4.3 propeller, the same effect occurs at propeller advance ratios of 0.70 and 0.61.

3. *Reynolds Number Effects*

To exhibit the relationship of the Reynolds number on the performance of the Wortmann wing for a fixed propeller rotation rate, the lift-to-drag ratio curves of the GWS 5 × 4.3 (8000 rpm) and GWS 3 × 3 (12,000 rpm) propellers in the tractor and pusher configurations at Reynolds numbers between 60,000 and 90,000 are presented in Figs. 21 and 22. In addition, the percentage increase in $(C_L/C_D)_{max}$ from the clean configuration at each Reynolds number is tabulated in Table 5. The results shown in Figs. 21 and 22 are somewhat counterintuitive because an increase in the advance ratio shows higher absolute lift-to-drag ratios. However, Table 5 correctly shows a decrease in $\Delta(C_L/C_D)_{max}$ from the corresponding clean configuration with an increase in J (decrease in w). For all Reynolds numbers tested, the tractor configuration results exhibit the wing's ability to reach higher lift-to-drag ratios, even at low angles of attack. In addition, even with the separation bubble already attached in the clean configuration like the Reynolds number Re of 90,000 case, the tractor configuration propeller results in a higher lift-to-drag ratio for the wing as compared with the pusher configuration. This increase is true despite the GWS 5 × 4.3 propeller operating in the windmill-brake state because J is larger than 0.8.

4. *Constant T/A Comparison*

The type of propeller used on an aircraft is determined based on its performance characteristics (T, T/A, C_T, C_Q, and η), overall aircraft characteristics and constraints, and mission-specific requirements. The question is whether there are varied effects on wing performance for different types of propellers (tractor configuration) with a constant disk loading (constant T/A). A constant T/A directly translates to a constant induced flow w from the propeller. The difference lies in the swirl (tangential component) of the slipstream. For a propeller that is centered on the wing, this means that one side of the wing sees an increase in the local angle of attack and the opposite side of the wing sees an equal reduction in the local angle of attack. However, in terms of the total lift and downwash characteristics of the wing, these effects mostly cancel out. Figures 23a and 23b show a comparison of lift and drag curves for the various 5 in. (127 mm) diameter propellers tested with the Wortmann wing at a Reynolds number of 60,000 at a constant T/A of 0.16. For a constant T/A setting, the wing lift and drag vary minimally with the propeller pitch and number of blades.

Lift and drag curve comparisons are also performed for GWS propellers of varying diameters [3.2, 4, and 5 in. (81.3, 101.6, and 127 mm)] operating at a constant T/A of 0.16 (see Figs. 24a and 24b). Unlike the 5 in. (127 mm) propeller comparisons, for this case, the lift and drag performance of the wing varies because the portion of the wing within the induced flow of the propeller changes. What can be observed from the lift and drag curves is that the separation bubble formation occurs at lower angles of attack with increasing propeller diameter. As discussed in Sec. III.C.1, dynamic pressure effects, local changes in angle of attack, and the tripping effect of the propeller slipstream all play a part in the differences observed in the wing performance. The GWS 3 × 3 propeller case has the lowest $C_{L_{max}}$ and

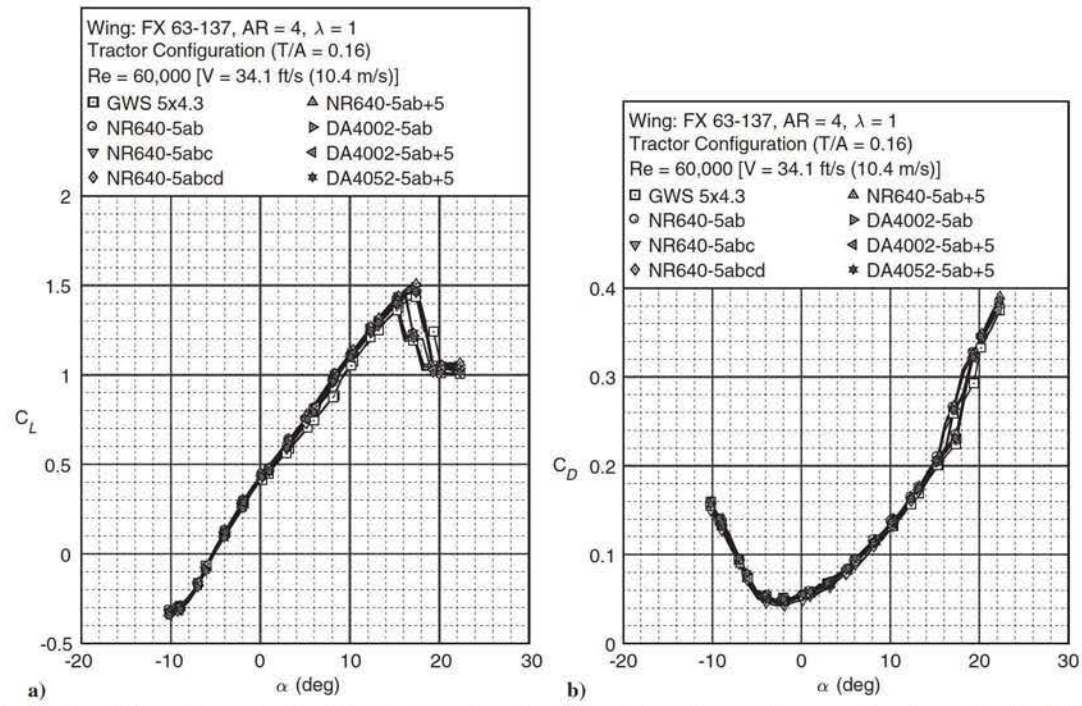

Fig. 23 Wortmann wing at Reynolds number Re of 60,000 with various 5 in. (127 mm) diameter propellers operating at a constant T/A (constant induced flow) of 0.16: a) lift curve, and b) drag curve.

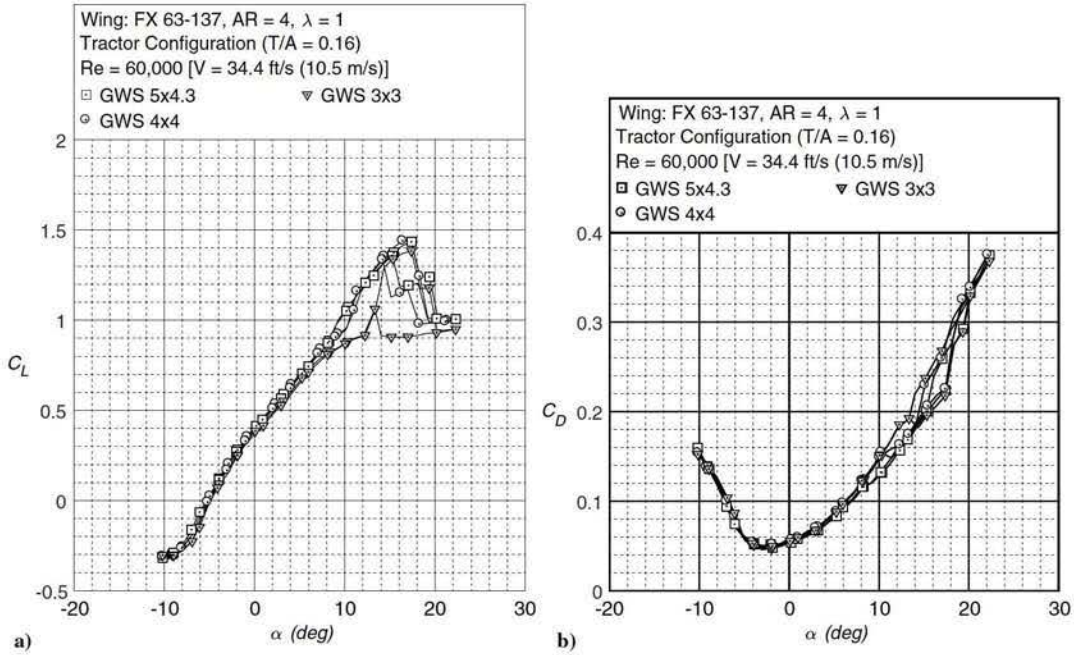

Fig. 24 Wortmann wing at Reynolds number *Re* of 60,000 with 3.2, 4, and 5 in. (81.3, 101.6, and 127 mm) GWS propellers operating at a constant T/A of 0.16: a) lift curve, and b) drag curve.

shows bubble formation at a higher angle of attack as compared with the GWS 4 × 4 and GWS 5 × 4.3 propellers. Similarly, for the GWS 4 × 4, the formation of the separation bubble occurs at a higher angle of attack as compared with the GWS 5 × 4.3 propeller. The drag drop (see Fig. 24b) observed at higher angles of attack also only occurs for the two larger-diameter propellers and is not evident for the GWS 3 × 3 propeller.

IV. Conclusions

A review of the literature suggested that, in the low-Reynolds-number (30,000 to 80,000) low- to moderate-aspect-ratio wing ($2 \leq \mathcal{R} \leq 5$) regime, there was a lack of data that related to the effect of the induced flow of a propeller on the performance of a wing. A majority of the small-scaled fixed-wing UAVs operated with a significant portion of their wing located in the slipstream of the propeller. Therefore, an experimental setup was created that allowed for different parameters related to the propeller location (tractor or pusher) and advance ratio J with respect to the wing to be tested easily.

The experiments presented in the paper were done using the Wortmann FX 63-137 rectangular wing with an aspect ratio of four and multiple 3, 4, and 5 in. (76.2, 101.6, and 127 mm) diameter propellers in the pusher and tractor configurations. Results were presented for the effects of varying the propeller advance ratio, varying the wing chordwise Reynolds number, and the constant propeller T/A. An important conclusion that was drawn from the results obtained was that a large performance benefit (C_L/C_D) was found for the Wortmann wing under propeller slipstream conditions (tractor configuration). From oil flow visualization results, it was observed that the induced flow due to the propeller created a region of fully turbulent flow on the central portion of the wing and induced the formation of the separation bubble over the rest of the wing at lower chordwise Reynolds numbers. In addition to a local flow velocity (dynamic pressure) increase and change in the local angle of attack, the region of turbulent flow attenuated the pressure drag and increased the lift of the wing at angles of attack up to stall. In essence, the induced flow due to the propeller acted as a trip that most importantly worked at both low angles of attack and when the propeller was in a brake state ($w = 0$). Significant performance benefits were not observed for the propeller in the pusher configuration, however. In the pusher configuration, the induced flow due to the propeller increased the local freestream velocity and decreased the local angle of attack over the wing, thereby delaying the laminar separation point. Lastly, in the tractor configuration, with a constant induced flow setting, wing performance was minimally affected by the number of propeller blades and the blade pitch. What was important, though, was the diameter of the propeller. Larger-diameter propellers exhibited significant wing performance (lift-to-drag ratio) benefits as compared with smaller-diameter propellers.

The results presented in this paper show that the performance of a low-Reynolds-number wing with a propeller in the tractor configuration produces as much a 70% increase in the lift-to-drag ratio from the clean configuration. These benefits are not observed for the propeller in the pusher configuration. The benefits found from the experiments performed on the Wortmann wing can be translated to improved small-scale and high-altitude long-endurance UAV performance at most flight conditions (takeoff, cruise, and landing).

Acknowledgments

The authors thank Pritam P. Sukumar, Jeff Diebold, or D. Dantsker, and Raylan Vaz for their assistance in wind-tunnel testing. The authors would also like to thank Scott A. McDonald, Greggory L. Bennett, and David L. Switzer from the University of Illinois at Urbana–Champaign Electrical and Computer Engineering machine shop for their guidance and support in machining the three-component platform force balance.

References

[1] Smelt, R., and Davies, H., "Estimation of Increase in Lift due to Slipstream," R&M 1788, Aeronautical Research Council, United Kingdom, 1937.

[2] Young, A. D., and Morris, D. E., "Note of Flight Tests on the Effect of Slipstream on Boundary Layer Flow," R&M 1957, Aeronautical Research Council, United Kingdom, 1939.

[3] Young, A. D., and Morris, D. E., "Further Note of Flight Tests on the Effect of Slipstream on Boundary Layer Flow," Rept. B.A. 1404b, Royal Aeronautical Establishment, United Kingdom, 1939.

[4] Thompson, J. S., Smelt, R., Davison, B., and Smith, F., "Comparison of Pusher and Tractor Propeller Mounted on a Wing," R&M 2516, Aeronautical Research Council, United Kingdom, 1940.

[5] Kuhn, R. E., and Draper, J. W., "Investigation of the Aerodynamic Characteristics of a Model Wing-Propeller Combination and of the Wing and Propeller Separately at Angles of Attack up to 90 deg," NACA Rept. 1263, 1956.

[6] Brenkmann, M., "Experimental Investigation of the Aerodynamics of a Wing in a Slipstream," Rept. 11, Univ. of Toronto Inst. for Aerospace Studies, Toronto, April 1957.

[7] Ribner, H. S., "Theory of Wings in Slipstreams," Rept. 60, Univ. of Toronto Inst. for Aerospace Studies, Toronto, May 1959.

[8] Loth, J. L., and Loth, F., "Induced Drag Reduction with Wing Tip Mounted Propellers," *2nd AIAA Applied Aerodynamics Conference*, AIAA Paper 1984-2149, Aug. 1984.

[9] Patterson, J. C., and Barlett, G. R., "Effect of a Wing-Tip Mounted Pusher Turboprop on the Aerodynamic Characteristics of a Semi-Span Wing," *21st AIAA/SAE/ASME/ASEE Joint Propulsion Conference*, AIAA Paper 1985-1286, July 1985.

[10] Miranda, L., and Brennan, J., "Aerodynamic Effects of Wingtip-Mounted Propellers and Turbines," *4th AIAA Applied Aerodynamics Conference*, AIAA Paper 1986-1802, July 1986.

[11] Kroo, I., "Propeller-Wing Integration for Minimum Induced Loss," *Journal of Aircraft*, Vol. 23, No. 7, 1986, pp. 561–565. doi:10.2514/3.45344

[12] Munk, M., "Minimum Induced Drag of Airfoils," NACA Rept. 121, 1921.

[13] Veldhuis, L. L. M., "Review of Propeller-Wing Aerodynamic Interference," *Proceedings of the 24th International Congress of the Aeronautical Sciences*, ICAS Paper 2004-6.3.1, Yokohama, Japan, 2004.

[14] Veldhuis, L. L. M., "Propeller-Wing Aerodynamic Interference," Ph.D. Dissertation, Dept. of Aerospace Engineering, Delft Univ. of Technology, Delft, The Netherlands, June 2005.

[15] Witkowski, D. P., Johnston, R. T., and Sullivan, J. P., "Propeller/Wing Interaction," AIAA Paper 1989-0535, 1989.

[16] Witkowski, D. P., Lee, A. K. H., and Sullivan, J. P., "Aerodynamic Interaction Between Propellers and Wings," *Journal of Aircraft*, Vol. 26, No. 9, 1989, pp. 829–836. doi:10.2514/3.45848

[17] Catalano, F. M., "On the Effect of an Isolated Propeller Slipstream on Wing Aerodynamic Characteristics," *Acta Polytechnica*, Vol. 44, No. 3, 2004, pp. 8–14.

[18] Pines, D. J., and Bohorquez, F., "Challenges Facing Future Micro-Air-Vehicle Development," *Journal of Aircraft*, Vol. 43, No. 2, March–April 2006, pp. 290–305. doi:10.2514/1.4922

[19] Null, W., Noseck, A., and Shkarayev, S., "Effects of Propulsive-Induced Flow on the Aerodynamics of Micro Air Vehicles," *23rd AIAA Applied Aerodynamics Conference*, AIAA Paper 2005-4616, June 2005.

[20] Shkarayev, S., Moschetta, J.-M., and Bataille, B., "Aerodynamic Design of Micro Air Vehicles for Vertical Flight," *Journal of Aircraft*, Vol. 45, No. 5, Sept.–Oct. 2008, pp. 1715–1724. doi:10.2514/1.35573

[21] Randall, R., Hoffmann, C.-A., and Shkarayev, S., "Longitudinal Aerodynamics of a Vertical Takeoff and Landing Micro Air Vehicle," *Journal of Aircraft*, Vol. 48, No. 1, Jan.–Feb. 2011, pp. 166–176. doi:10.2514/1.C031044

[22] Randall, R., Wilson, L., and Shkarayev, S., "Flow Interactions Around a Rapidly-Pitching MAV Wing," *50th AIAA Aerospace Sciences Meeting and Exhibit*, AIAA Paper 2012-0667, Jan. 2012.

[23] Sudhakar, S., Kumar, C., Arivoli, D., Dodamani, R., and Venkatakrishnan, L., "Experimental Studies of Propeller Induced Flow over a Typical Micro Air Vehicle," *51st AIAA Aerospace Sciences Meeting and Exhibit*, AIAA Paper 2013-0060, Jan. 2013.

[24] Selig, M. S., and McGranahan, B. D., "Wind Tunnel Aerodynamic Tests of Six Airfoils for Use on Small Wind Turbines," Rept. NREL/SR-500-34515, National Renewable Energy Lab., Golden, CO, 2004.

[25] Ananda, G. K., "Aerodynamic Performance of Low-to-Moderate Aspect Ratio Wings at Low Reynolds Numbers," M.S. Thesis, Dept. of Aerospace Engineering, Univ. of Illinois at Urbana–Champaign, Urbana, IL, 2012.

[26] Ananda, G. K., Sukumar, P. P., and Selig, M. S., "Measured Aerodynamic Characteristics of Wings at Low Reynolds Numbers," *Aerospace Science and Technology*, Vol. 42, April–May 2015, pp. 392–406. doi:10.1016/j.ast.2014.11.016

[27] Barlow, J. B., Rae, W. H., Jr., and Pope, A., *Low-Speed Wind Tunnel Testing*, 3rd ed., Wiley, New York, 1999.

[28] Kline, S., and McClintock, F. A., "Describing Uncertainty in Single-Sample Experiments," *Mechanical Engineering*, Vol. 75, 1953, pp. 3–8.

[29] Coleman, H. W., and Steele, W. G., Jr., *Experimentation and Uncertainty Analysis for Engineers*, Wiley, New York, 1989.

[30] Anon., "Realize, Inc., Rapid Prototyping, Rapid Prototypes, Stereolithography," http://www.realizeinc.com/ [retrieved Feb. 2012].

[31] Deters, R. W., Ananda, G. K., and Selig, M. S., "Reynolds Number Effects on the Performance of Small-Scale Propellers," *32nd AIAA Applied Aerodynamics Conference, AIAA AVIATION Forum*, AIAA Paper 2014-2151, June 2014.

[32] Deters, R. W., "Performance and Slipstream Characteristics of Small-Scale Propellers at Low Reynolds Numbers," Ph.D. Dissertation, Dept. of Aerospace Engineering, Univ. of Illinois at Urbana–Champaign, Urbana, IL, Jan. 2014.

[33] Brandt, J. B., "Small-Scale Propeller Performance at Low Speeds," M.S. Thesis, Dept. of Aerospace Engineering, Univ. of Illinois at Urbana–Champaign, Urbana, IL, 2005.

[34] Deters, R. W., Ananda, G. K., and Selig, M. S., "Slipstream Measurements of Small-Scale Propellers at Low Reynolds Numbers," *33rd AIAA Applied Aerodynamics Conference, AIAA AVIATION Forum*, AIAA Paper 2015-2265, June 2015.

[35] Ananda, G. K., Sukumar, P. P., and Selig, M. S., "Low-to-Moderate Aspect Ratio Wings Tested at Low Reynolds Numbers," *30th AIAA Applied Aerodynamics Conference*, AIAA Paper 2012-3026, June 2012.

[36] Tani, I., "Low-Speed Flows Involving Bubble Separations," *Progress in Aerospace Sciences*, Vol. 5, 1964, pp. 70–103. doi:10.1016/0376-0421(64)90004-1

[37] Selig, M. S., Guglielmo, J. J., Broeren, A. P., and Giguère, P., *Summary of Low-Speed Airfoil Data*, Vol. 1, SoarTech Publ., Virginia Beach, VA, 1995.

[38] Selig, M. S., "The Design of Airfoils at Low Reynolds Numbers," *23rd AIAA Aerospace Sciences Meeting and Exhibit*, AIAA Paper 1985-0074, Jan. 1985.

[39] Althaus, D., *Profilpolaren für den Modellflug (Windkanalmessungen an Profilen im Kritischen Reynoldszahlbereich)*, Necker-Verlag, Villingen-Schwenningen, Germany, 1980.

[40] Mueller, T. J., "Low Reynolds Number Vehicles," AGARDograph No. 288, NATO Advisory Group for Aerospace Research and Development, Neuilly Sur Seine, France, Feb. 1985.

[41] Bastedo, W. G., Jr., and Mueller, T. J., "Spanwise Variation of Laminar Separation Bubbles on Wings at Low Reynolds Numbers," *Journal of Aircraft*, Vol. 23, No. 9, Sept. 1986, pp. 687–694. doi:10.2514/3.45363